University of Wisconsin Milwaukee
UWM Digital Commons

Theses and Dissertations

December 2014

An Analysis of CO2-driven Cold-water Geysers in Green River, Utah and Chimayo, New Mexico

Zachary T. Watson
University of Wisconsin-Milwaukee

Follow this and additional works at: https://dc.uwm.edu/etd

Part of the Geology Commons, and the Hydrology Commons

Recommended Citation

Watson, Zachary T., "An Analysis of CO2-driven Cold-water Geysers in Green River, Utah and Chimayo, New Mexico" (2014). *Theses and Dissertations*. 603.
https://dc.uwm.edu/etd/603

This Thesis is brought to you for free and open access by UWM Digital Commons. It has been accepted for inclusion in Theses and Dissertations by an authorized administrator of UWM Digital Commons. For more information, please contact open-access@uwm.edu.

AN ANALYSIS OF CO_2-DRIVEN COLD-WATER GEYSERS IN GREEN RIVER, UTAH AND CHIMAYO, NEW MEXICO

by

Zach Watson

A Thesis Submitted in

Partial Fulfillment of the

Requirements for the Degree of

Master of Science

Geosciences

at

The University of Wisconsin-Milwaukee

December 2014

ABSTRACT

AN ANALYSIS OF CO_2-DRIVEN COLD-WATER GEYSERS IN UTAH AND NEW MEXICO

by

Zach Watson

The University of Wisconsin-Milwaukee, 2014
Under the Supervision of Professor Dr. Weon Shik Han

The eruption periodicity, CO_2 bubble volume fraction, eruption velocity, flash depth and mass emission of CO_2 were determined from multiple wellbore CO_2-driven cold-water geysers (Crystal and Tenmile geysers, in Utah and Chimayó geyser in New Mexico). Utilizing a suite of temporal water sample datasets from multiple field trips to Crystal geyser, systematic and repeated trends in effluent water chemistry have been revealed. Crystal geyser has a four part eruption cycle composed of a minor eruption period (mEP), major eruption period (MEP), aftershock eruption period (Ae) and recharge (R). Tenmile geyser has a four part eruption cycle composed of MEP, drainage (D), mEP and R. Chimayó geyser has a two part eruption cycle composed of a MEP and R. The MEP at Crystal geyser currently lasts for over 24 hours highlighting the potential for a natural geyser to reach quasi steady state discharge. At shallow depths the bubble volume fraction ranges from 0 to 0.8, eruption velocities range from 2 to 20 m/s and flash depths are predominately shallow ranging from 5 to 40 meters below the surface. Annual emission of CO_2 is estimated to be $(4.77\pm1.92)\times10^3$, $(6.17\pm1.73)\times10^1$, $(6.54\pm0.57)\times10^1$ tonnes/yr for Crystal, Tenmile and Chimayó geysers, respectively. Inverse modeling of endmembers for the mEP at Crystal geyser show that the effluent is comprised of 66%, 33% and 1% the Navajo Sandstone, Entrada Sandstone and Fault Brine, respectively. The range of input for the Navajo, Entrada and Brine during the MEP is 53-57%, 42-45% and 1-2%, respectively. The geyser plumbing geometry consists of a vertical wellbore which allows for the upward migration of CO_2-rich fluids due to artesian conditions. The positive feedback system of a CO_2-driven eruption occurs within the well. Mitigating high velocity CO_2-driven discharge from wellbores will, however, be easier than mitigating diffuse leakage from faults or into groundwater systems.

TABLE OF CONTENTS

LIST OF FIGURES

LIST OF TABLES

ACKNOWLEDGEMENTS

The biggest thanks of all must go to Dr. Weon Shik Han for everything he did for me. He took me on as an undergraduate with a lousy transcript, gave me a chance and it blossomed into nearly three years of research. His dedication to his work and students is unparalleled; he serves as the exemplar of all advisors and scientists. In fact, he's the James Brown of geoscientists. I'd like to thank Tim Grundl for sharing his knowledge of water chemistry and putting up with me asking endless random questions. Thanks to Barry Cameron for joining my committee and always making me feel positive about the research I've done. Thanks to the UWM Geoscience office department (Chris, Lisa, Julianna, Adrianna and Lynn) for all of their help. Thanks to Patrick Anderson at the School of Freshwater Sciences for his help with major ion analyses of my geyser water samples. Thanks to Niko Kampman at Lancaster University, Shaul Hurwitz at the USGS and the other anonymous reviewers of my papers. While their suggestions or rejections were a source of frustration, the quality of my thesis would not be what it is without their input. An additional thanks to Niko Kampman for sharing his data with us, the collaboration has significantly advanced our understanding of Crystal geyser. Thanks to Meng Lu at CSIRO for providing his knowledge and code for simulating CO_2-driven geysering processes. I'd like to thank Jack Graham, Cheng Thao and Aaron Ziegler for their assistance in the field. Thanks to Na-Hyun Jung for reviewing/editing my papers and helping with submission processes. Thanks to Kyung-Doe Han for his help with water analysis and table creation. More thanks should go to Jack Graham and Ethan Guyant for putting up with my "while-listening-to-music" antics in the office. Finally I'd like to thank my parents for putting me through college and getting me to the point to where I could return the favor by continuing my education not on their dime.

1. Introduction to CO_2-Driven Cold-Water Geysers

Thermally driven geysers, like Old Faithful in Yellowstone, are characterized by periodic eruptions of liquid water and steam (Kieffer, 1989; Nicholl et al., 1994). Conventional subsurface structures are composed of a long conduit connected to a large chamber at the base (Hurwitz et al., 2012; Hutchinson et al., 1997; Kieffer, 1989; Rinehart, 1980; Vandemeulebrouck et al., 2013). Heating of liquid water in the chamber combined with the non-convective properties of the conduit provide the rapid feedback process of an eruption (Rinehart, 1980). Another potential subsurface structure capable of producing periodic thermally driven eruptions was recently revealed by Belousov et al. (2013). Large porous structures trap steam until the pressure of steam within the trap is greater than that of the liquid water pressure in the conduit. When the eruption is initiated, the steam immediately releases into the conduit and buoyantly accelerates producing an eruption at the surface. Like thermally driven geysers, CO_2-driven cold-water geysers also have conduits as a necessary part of their structure. The conduit in the case of CO_2-driven geysers is typically a manmade wellbore (Glennon and Pfaff, 2005). Furthermore, although both cold and hot water geysers are driven by a gas expansion process, gas evolves differently in cold-water geysers. Temperatures within CO_2-driven cold-water geysers always remain below the boiling point of liquid water. In CO_2-driven geysers, $CO_{2(g)}$ evolves by the pressure reduction (flashing) of CO_2-rich fluids (Lu et al., 2005), not by boiling. Once the internal pressure of $CO_{2(aq)}$ becomes greater than that of the surrounding fluid ($P_{CO2} > P_{fluid}$), CO_2 exsolves causing bubbles to nucleate, grow and coalesce. Reduction of hydrostatic pressure resulting from increasing CO_2 bubble volume fraction within the wellbore enhances expansion of CO_2 bubbles while the conduit walls constrict lateral growth leading to the surface eruption.

1.1 Introduction to Geologic Carbon Storage

Growing interest in geologic carbon storage (GCS) has brought attention to CO_2-driven cold-water geysers because of its similarity to high velocity wellbore leakage processes (Gouveia et al., 2005; Jordan and Benson, 2009; Oldenburg, 2011; Shipton et al., 2004). GCS has been proposed as a viable method for reducing atmospheric CO_2 emissions. GCS consists of separating CO_2 at power plants, compressing and then injecting it into highly permeable rock units at depths great enough to keep CO_2 in a supercritical state. Depleted oil and gas formations will be the primary target areas for GCS due to their shown ability to trap gases and fluids for geologic time periods. Successful storage requires that no more than 0.1% of the annual injected CO_2 leaks from the storage formation (IPCC, 2005). At the ideal pressure and temperature conditions, CO_2 will be in a buoyant supercritical state. Targeting anticlinal like structures will provide geometries which further constrain the migration of CO_2. However, the buoyancy of CO_2 will also drive upward migration through permeable networks or wells if they exist. Dissolution of caprock minerals by acidic CO_2-rich fluids may also generate permeable pathways for CO_2 to escape through. The various expressions of CO_2 leakage in form of contaminated aquifers, geysering wellbores, travertine mounds and anomalous surface CO_2 flux provide researchers with a suite of data to use in determining why CO_2 is leaking and what could be seen if CO_2 is leaking from a GCS facility. Most studies on carbon storage have focused on large scale diffuse leakage through faults or the near surface (Allis et al., 2005; Burnside et al., 2013; Jung et al., 2014; Lewicki et al., 2003; Shipton et al., 2004). However, many studies emphasized that the leakage rate of CO_2 from naturally leaking sites is greatest through geysering wellbores (Bickle and Kampman, 2013; Burnside et al., 2013; Shipton et al., 2004). Depending upon spatial density of wells, hundreds of wells could potentially be impacted by a single CO_2 plume in commercial-scale demonstrations (Celia et al., 2004). The density of wellbores in Alberta, Canada has been shown to reach 4 wells per km^2 in areas of higher density. With an estimated 5 km radial extent of a CO_2 plume, 312 wells could be in direct contact at depth. Geysering within wells could: (1) vent CO_2 as a free gas into the atmosphere (Han et al., 2013), (2) discharge brine which could potentially contaminate the surface (Hu et al., 2012) and (3) enhance mixing between potable water in shallow aquifers and saline brine (Keating et al., 2010). The uncertainties surrounding the potential for wellbores to develop into geysers demands an analysis of naturally occurring CO_2-driven geysers (Celia et al., 2004; Friedmann, 2007). Therefore, this study provides *in-situ* measurements of pressure and temperature from three CO_2-driven cold-water geysers (Crystal and Tenmile geysers in Utah and Chimayó geyser in New Mexico) and elucidates the sequential processes of in-well $CO_{2(g)}$ occupation, eruption velocity, CO_2 flashing depths and annual CO_2 emission rate. A conceptual model and numerical simulation of the CO_2-driven geysering process is presented with implications to leakage of geologic carbon storage.

2. Field Sites of CO_2-Driven Cold-Water Geysers

2.1 Green River, Utah

The sedimentary basins of Green River, Utah and Chimayó, New Mexico have become prominent field laboratories for GCS analogue studies due to the naturally leaking CO_2 through faults, springs and wellbores (Han et al., 2013; Heath et al., 2009; Kampman et al., 2009; Kampman et al., 2014; Keating et al., 2010; Shipton et al., 2005). The Colorado Plateau is host to numerous accumulations of natural gas, oil and CO_2. Green River, Utah lies in the northernmost extent of the Paradox Basin consisting of Pennsylvanian to Jurassic sediments. The north-plunging Green River Anticline intersects the east-west trending Little Grand Wash (LGW) and Salt Wash (SW) fault systems. The LGW fault is a south dipping fault comprised of two parallel strands with a total vertical separation of 180-210 m (Shipton et al., 2005). The total penetration depth of the LGW fault system is unknown. Further to the south is the SW fault system which consists of two northwest striking normal faults. The faults are separated by 15 km forming the Salt Wash/Tenmile Graben. Like the LGW, the depth that the SW fault extends to is unknown. The fault systems act as both conduits and barriers to the flow of CO_2 and brine to the surface and shallow aquifers. Carbonate travertine deposits overlie ancient CO_2 leakage points. U-Th age dating of travertine deposits in this region indicate that CO_2 has been leaking for at least 400,000 years where rates increased during periods of climatic warming (Burnside et al., 2013; Kampman et al., 2012). The CO_2 originated from thermal decomposition of marine carbonates, specifically the Mississippian Leadville Limestone (Kampman et al., 2009; Shipton et al., 2004). Brine and CO_2

migrate upward along the fault systems to enter the shallow groundwater systems. The emitted gas exceeds 95% CO_2 for all Green River springs and geysers with the remaining percentage composed of atmospheric gases N_2, O_2 and Ar (Heath et al., 2009). The isotopic $\delta^{13}C$ values of $CO_{2(g)}$ range from -6.61 to -7.55 per mil for the springs and geysers in the Green River region inferring a shared origin (Heath et al., 2009; Kampman et al., 2009). The primary aquifers are the Jurassic aged Entrada and Navajo Sandstones. The Entrada Sandstone is exposed at the surface of Crystal geyser and Tenmile geyser and reaches a depth of 150 m where it meets the impermeable Carmel Formation. Below the Carmel Formation is the most productive unit, the Navajo Sandstone which occurs at a depth of 200-320 m (Kampman et al., 2014). Precipitation and snowmelt to the Northwest in the San Rafael Swell recharges these units on the order of 1.23×10^7 m^3/yr where roughly 30% (3.7×10^6 m^3/yr) of this recharges the Navajo Sandstone, equivalent to 9 mm/yr (Hood and Patterson, 1984). The elevated recharge zone produces artesian conditions throughout the Green River area resulting in formation overpressures ranging from 0-5 bars for the aforementioned Jurassic formations (Kampman et al., 2014). Crystal geyser is an abandoned oil exploration well (Glen Ruby#1-X) drilled during the mid-1930’s along the north side of the east-west striking Little Grand Wash fault (Fig. 1A). The total depth of the well is ~800 m, only cased at the surface with a height of 1.73 m above the ground surface and diameter of 0.39 m. A blockage of rocks was observed at ~6 m depth. Tenmile geyser, also an abandoned oil exploration well, is located south-east of Crystal geyser on the hanging wall of the Salt Wash Graben (Fig. 1A). The depth is unknown; a 1 m high and 0.23 m diameter casing rests at the surface. A camera was sent into the well reaching a depth of ~45 m where a clog of rocks and sticks prevented any further penetration.

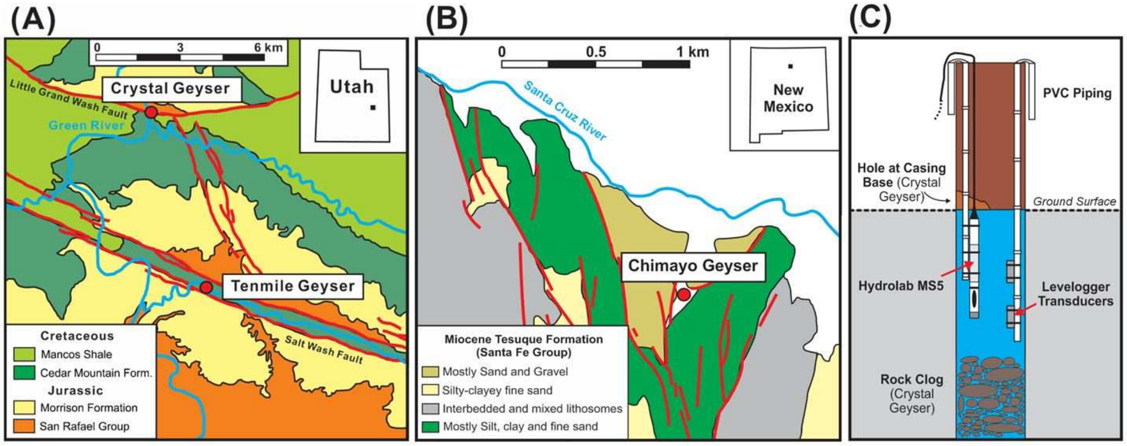

Figure 1. Map of Green River, Utah and Chimayó, New Mexico. (A) The location of Crystal and Tenmile geysers (red dots) in Utah and (B) the location of Chimayó geyser in New Mexico. Faults are shown as red lines. Utah and New Mexico maps are modified from Kampman et al. (2009) and Keating et al. (2010), respectively. (C) Schematic diagram of well configuration and transducer installation.

2.2 CO_2-driven Springs and Geysers in Green River, Utah

All of the CO_2-driven springs and geysers except for Crystal geyser lie along or nearer to the SW fault. The four known CO_2-driven springs are Small and Big Bubbling, Pseudo-Tenmile and Torrey's spring which consist of cool waters (13-18 ºC) bubbling continuously forming small travertine deposits at the surface. The travertine deposits surrounding the springs are typically yellow to red in color due to the presence of hematite (Fe_2O_3). The mineralogical structure is poorly formed in comparison to the aragonite veins which make up the large travertine mounds elsewhere. Torrey's Spring is located along the footwall of the Northern SW fault. The surrounding travertine mound radially extends 7 m around the emanating point (Shipton et al., 2005). The largest of all the springs is Big Bubbling spring which extends radially some 10-15 m. Unlike the springs, all of the geysers originate from man-made wellbores either initially for residential use or natural gas exploration. The only geyser within the SW Graben is Tenmile geyser and it is analyzed extensively later in the paper. To the southwest of Tenmile geyser is Tumbleweed geyser. Tumbleweed geyser is essentially a small pond that erupts for periods of 46-94 minutes with quiet periods of 2-8.5 minutes (Glennon and Pfaff, 2005). It is said to be an abandoned wellbore but no drilling record is known to exist. Eruptions are mild reaching maximum heights of 2 m. Chaffin Ranch geyser, also referred to as Champagne geyser, was originally drilled in the 1930's by a homesteading family to the Southeast of Green River. A field trip to Chaffin Ranch geyser was conducted in June of 2013. Due to the small diameter of the opening (~ 2 cm), which may eventually be completely sealed by travertine, no instrumentation of the geyser was possible. The author arrived and waited ~2 hours before an eruption occurred. Preceding an eruption, water began to discharge rapidly for a few minutes. Then the eruption began discharging a $CO_{2(g)}$-water mixture to heights of 3 m. The day of observation was very windy and it is assumed that, on a calmer day, this geyser could send plumes to heights of 5 m. Eruptions at Chaffin Ranch geyser are the most gas dominated eruptions seen at any of the locations in Green River region where periods of the eruption consist only of the sound of CO_2 gas rushing out through the exit hole. The eruption continued erratically for 25 minutes, by which time the author ended observation. The mean length of an eruption is unknown. The witnessed duration of an eruption was much longer than cited by Glennon and Pfaff (2005) but the interval between eruptions was similar.

2.3 Chimayó, New Mexico

Chimayó Geyser is located in Chimayó, New Mexico within the Espanola Basin (Fig. 1B). The bedrock consists predominately of sandstones cut by north-south trending faults. Chimayó geyser lies near the Roberts Fault and may cut directly through it. The source of CO_2 is unknown for the region. The setting is similar to that of Green River, Utah where CO_2-rich brines migrate upward along faults (Keating et al., 2010). The regional aquifer supplying Chimayó geyser is semi-confined. The well was originally drilled in 1972 for residential water use but ended up tapping into a CO_2-rich water source and has geysered ever since. It has a diameter of 0.10 m, depth of 85 m and is cased with PVC for the entire depth.

2.4 Geyser Instrumentation

Each geysering well was instrumented with a pair of Solinst Levelogger Edge 3001 transducers to record the periodic changes in *in situ* pressure and temperature (Table 1). The transducers were attached to multiple 1.27 cm diameter PVC pipes connected to each other to prevent excessive vibration from the eruption activities (Fig. 1C). The transducer depths were selectively chosen due to accessibility (e.g., blockage of rocks within the well), and the measurement intervals were chosen between 10 to 60 seconds. Pressure and temperature measurements recorded by the transducers have an accuracy of ±0.05 kPa and ±0.05 ºC, respectively. Temperature measurements have a resolution of 0.003 ºC.

Table 1. Measurement date, depth, recording interval and total measurement time for each geyser.

	Measurement Depth (m)	**Recording Interval (s)**	**Total Measurement Time (Days)**
Crystal Geyser (12/8-16/2010)	6 and 14	20	8
Crystal Geyser (5/23 – 6/9/2013)	3 and 6	20	18
Tenmile Geyser (7/14-19/2011)	11.5 and 20.5	10	6
Tenmile Geyser (5/24 – 6/15/2013)	15 and 18	20	24
Chimayó Geyser (4/17 – 5/20/2008)	30.5 and 32	60	25

3. Previous Research Activities

The first research project on Crystal geyser was conducted in the 1970's with aims of preventing the geyser's saline waters from entering the Green River (Baer and Rigby, 1978). The first recording of the eruption periodicity by surficial measurements of pressure and temperature showed that Crystal geyser averaged 100 minutes of eruptive time per day and estimated the CO_2 emission to be 1.1×10^4 tonnes per year (Gouveia et al., 2005). Then Han et al. (2013) provided the first in-well measurements of pressure and temperature (14 and 6.5 m depth) revealing a consistent 6-part eruption cycle composed of minor and major eruptions and recharge periods. Unlike Crystal geyser, Tenmile geyser has received little attention due to its infrequent eruptions and difficult accessibility (Doelling, 1994; Ross, 1997). Water sampling of Tenmile geyser by Heath et al. (2009) and Kampman et al. (2009) revealed similarities to the water of Crystal geyser and surrounding Green River springs.

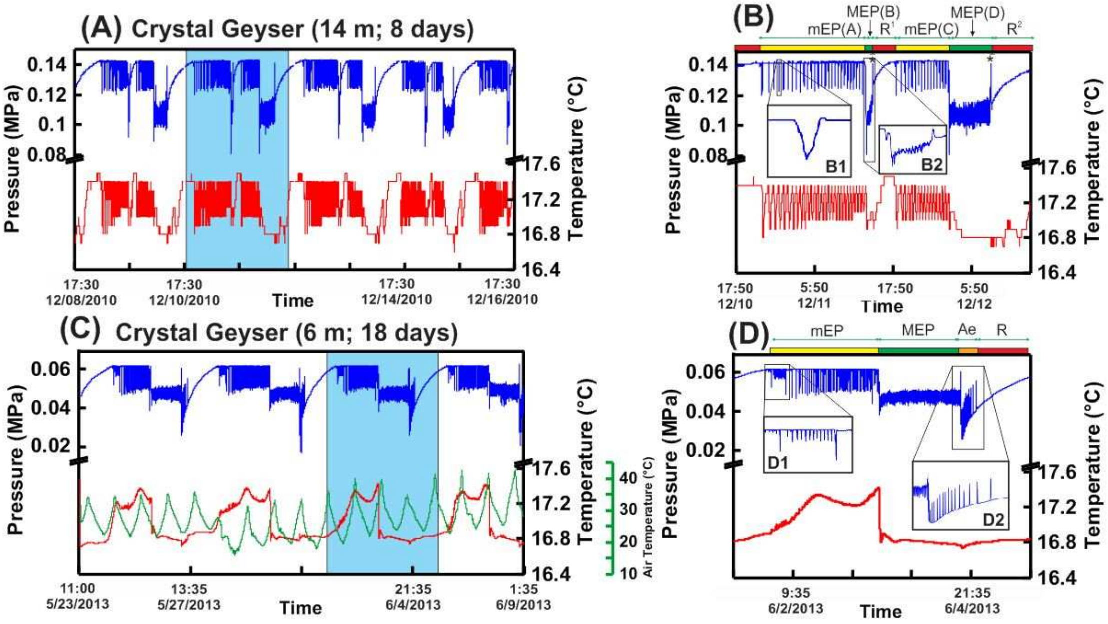

Figure 2. Variations of in situ pressure and temperature at Crystal geyser in (A) 2010 and (C) 2013. (B) and (D) Variations of pressure and temperature during a single eruption cycle from the blue highlighted region in (A) and (C), respectively. The yellow, green, orange and red bars bracket the times of mEP, MEP, Ae and R, respectively. Air temperature, shown in green in (C), at Crystal geyser. The selected period of B1 in (B) highlights the pressure change during a minor eruption and B2 highlights the pressure change during the MEP(B). The selected period of D1 in (D) denotes the minor bubbling event which initiates the mEP and D2 represents the Ae, which occur at the onset of the recharge period during observation in 2013.

4. Periodicity and Eruption Characteristics

4.1. Crystal Geyser: Measurements made in 2010 and 2013

Crystal geyser has a complex eruption cycle, which, in 2010, consisted of 6 parts averaging a net length of 41.4±5.2 hours (Fig. 2A and 2B). The total eruption cycle was made up of two minor eruption periods (mEP(A) and mEP(C)), two major eruption periods (MEP(B) and MEP(D)) and two recharge periods following the major eruptions (R^1 and R^2). The mEP(A) and mEP(C) had mean lengths of 13.2±2.1 and 6.8±1.4 hours, respectively, consisting of an average of 23.4±3.7 and 13.5±3.4 eruptions per period, respectively (Han et al., 2013). The mEP(A) and mEP(C) eruptions begin and end with CO_2 bubbling lasting 2 minutes each and the eruptions lasting 5 minutes with water emitted 2-3 m from the travertine surface. The average reduction in pressure and temperature at a depth of 14 m was approximately 0.018 MPa and 0.4 °C (17.5 °C to 17.1 °C), respectively. The time separating eruptions decreases throughout the period initially 40 minutes decreasing to 20 minutes prior to the major eruptions as shown in Figure 7 by Han et al. (2013). The MEP(B) and MEP(D) begin immediately as the final mEP(A) and mEP(C) end, respectively.

The MEP consists of a continuous and comparatively more intense eruption. Images of the MEP are shown in Fig. 3. The MEP(B) and MEP(D) had an average length of 1.1±0.1 and 6.0±0.5 hours, respectively. The sharp decrease in pressure (0.05 MPa) and temperature (0.6 ºC) denote the beginning of the major eruption. Eruption intensity is greatest at the onset with plumes reaching a height of 10 m. Specific to the MEP(B), pressure increases from 0.1 MPa to 0.12 MPa over the course of the period, corresponding to decreasing eruption vigor. In contrast, the MEP(D) has no loss in strength over the eruption period corresponding to a generally flat-lining pressure gradient. Oscillations of pressure within the eruption periods show the surges of both $CO_{2(g)}$ and liquid water, which appear as strong and weak eruptions at the surface (Fig. 2B). A portion of the discharged water remains pooled around the well during the eruption period and once the MEP ends this water drains directly back into the well. A few minutes after water has drained, well water rapidly rises (asterisk in Fig. 2B). Then the water level suddenly drops 1 and 2-2.5 m for MEP(B) and MEP(D), respectively. Recharge periods follow the major eruption periods, lasting 2.8 and 11 hours for the MEP(B) and MEP(D), respectively. Temperature reaches 17.4 ºC at the end of recharge, increasing 0.4 ºC and 0.6 ºC throughout the period following MEP(B) and MEP(D), respectively.

Instrumentation in 2013 revealed a new eruption periodicity of 4 parts; minor eruption period (mEP), major eruption period (MEP), aftershock eruptions (Ae) and recharge (R) (Fig. 2C and 2D). The total cycle is much longer, averaging a length of 102.9±5.1 hours. The mEP had a mean length of 40.6±6.4 hours. Unlike the mEP in 2010, the period now begins with ~15 small-scale bubbling events lasting 5.5±0.6 hours (D1 in Fig. 2D); the pressure reduction of individual bubbling events was less than 5 kPa. The individual eruptions during the mEP in 2013 are similar to those in 2010 with a length of ~9 minutes although eruption intensity has diminished; the eruption height is now ~1 m. The water level rises and falls at the beginning and the end of the minor eruption, respectively. Because the area surrounding the well is impermeable travertine, a portion of this water directly reenters the well. Due to water pooling during an eruption and then reentering the well afterwards, it is slightly warmed or cooled due to the current atmospheric temperature; seen in Fig. 2C where in-well temperature oscillates ~0.2 ºC during the mEP.

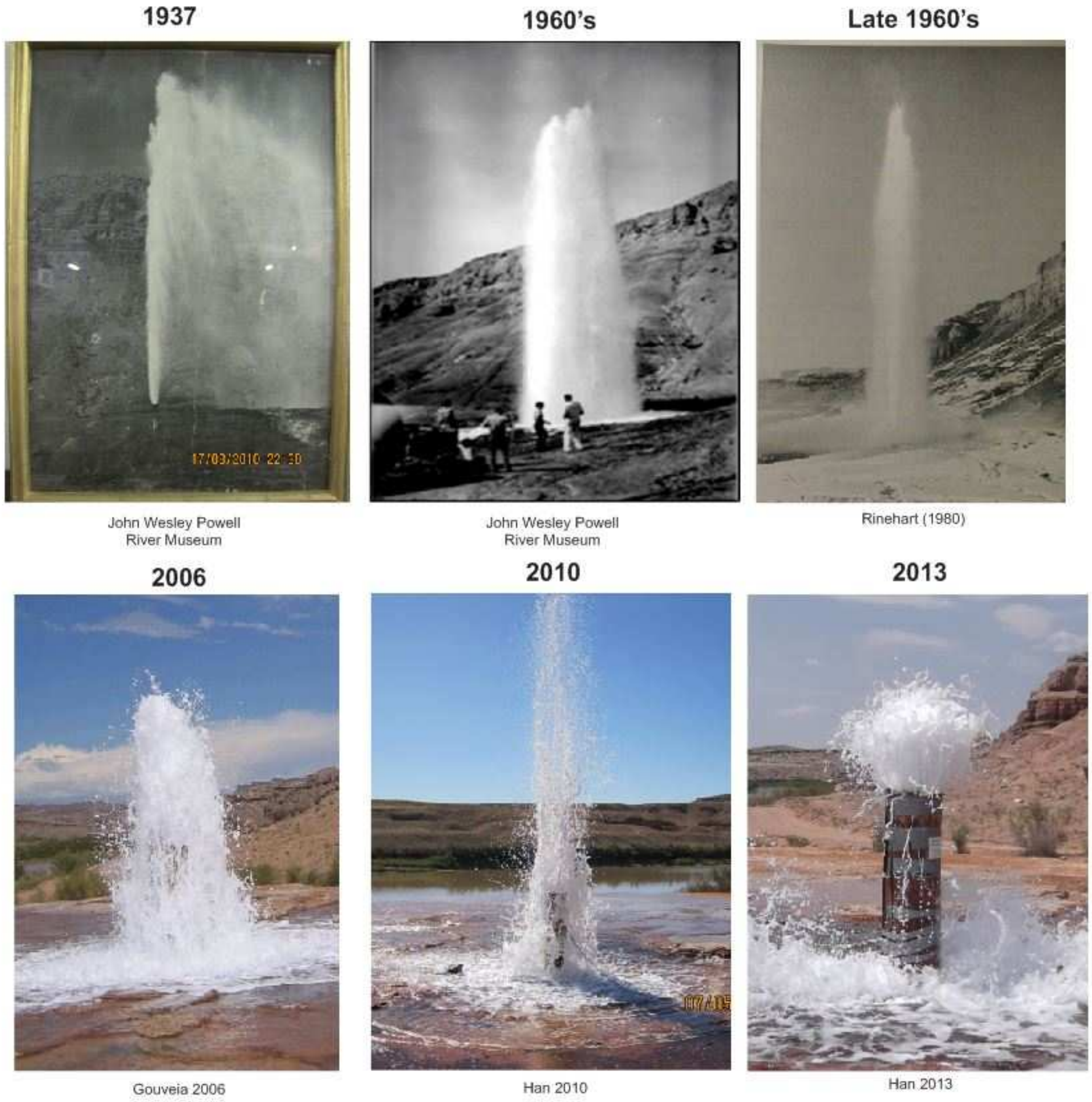

Figure 3. Photos of eruptions at Crystal geyser in 1937, the 1960's, the late 1960's, 2006, 2010 and 2013.

Like the MEP in 2010, the MEP in 2013 is a continuous and more intense eruption. Prior to the MEP, the discharge of liquid water from the well increases without degassing. Then, suddenly, large eruptions driven by $CO_{2(g)}$ slugs occur. The first 20-30 minutes of the MEP produce the highest erupting jets reaching a maximum height of 5 m in 2013; this can be seen in Fig. 2C and 2D where pressure dropped to 0.04 MPa at 6 m depth. The eruption continues discharging liquid water and CO_2 at heights of 1-3 m above the surface. Like the mEP, the MEP has also seen a significant increase in length averaging 27.3±0.5 hours in 2013. Temperature fluctuations follow the same pattern seen in 2010 with a sharp decrease from 17.4°C to 16.8°C (Han et al., 2013).

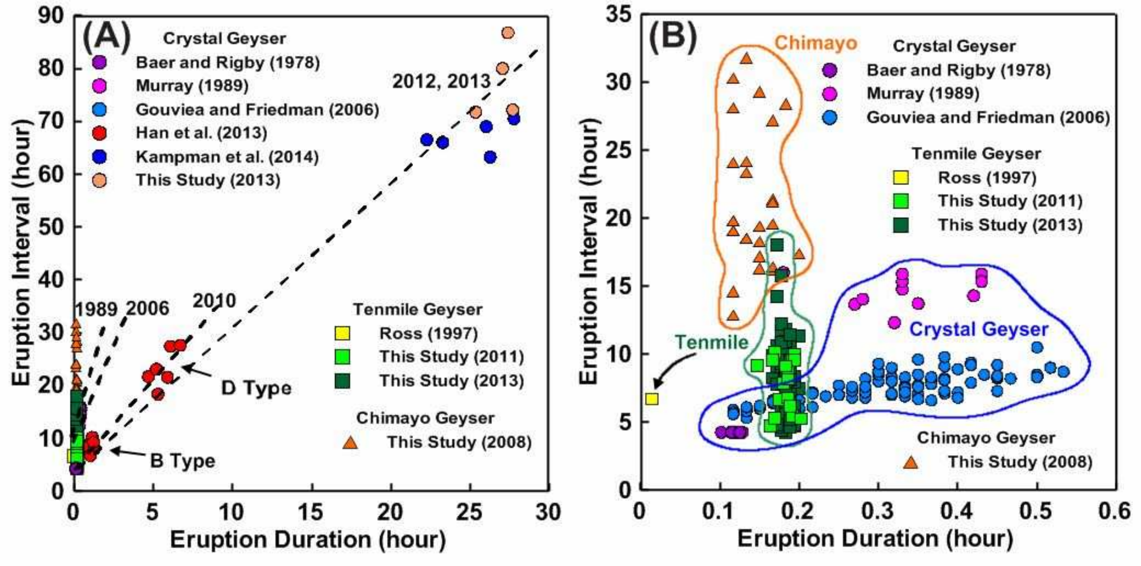

Figure 4. Comparison of interval to eruption length. (A) Eruption intervals and durations of Crystal, Tenmile, and Chimayó geysers with their trend (dashed) lines. (B) The magnified view of short eruption intervals and durations shown in (A). The 2010, 2012, and 2013 eruption interval and lengths at Crystal geyser are from Han et al. (2013), Kampman et al. (2014), and this study, respectively.

After water drains back into the well following the end of MEP, the aftershock eruption (Ae) period begins (D2 in Fig. 2D). This new eruption period was not observed in 2010 and is, essentially, the recharge period accompanied by eruptions only during the first few hours. Water is initially a few meters below the surface developing the minimum hydrostatic pressure condition and suddenly rises driven by CO_2 bubbles reaching the top of the well casing. The eruption lasts less than a minute initially and increases in length later. The first few Ae are of significantly greater intensity where later Ae are mild and predominately consist of the water level rising accompanied by minor CO_2 bubbling. Once the final Ae ends, recharge continues until the mEP begins.

The duration and intervals separating eruptions at Crystal geyser have shown considerable change over the 35 years of documentation (Fig. 4A and B). Similarly, Daisy Geyser and Old Faithful Geyser in Yellowstone National Park have shown variations diurnally, seasonally and annually (Hurwitz et al., 2014). Following nearby earthquakes, the intervals separating eruptions at Old Faithful Geyser increased. At Crystal geyser, the ratio of quiet time to eruptive time was 42:1 in 1978, decreasing to 7.5:1 in 2005 and 3:1 in 2013 corresponding to a continually decreasing vigor in eruptions (Baer and Rigby, 1978; Gouveia et al., 2005; Han et al., 2013). The reason for continuous changes in periodicity and intensity is unknown but could be due to reported dynamiting of the well (Shipton et al., 2004), growing rock obstructions, nearby seismic activity (Han et al., 2013), local drilling projects producing large quantities of CO_2-charged fluids, interactions between source aquifers and fault-controlled delivery rates of CO_2 to the aquifers (Kampman et al., 2014). Additionally, the geysering periods in 2013 were correlated with barometric pressure and earth tides revealing no connection during the measurement period.

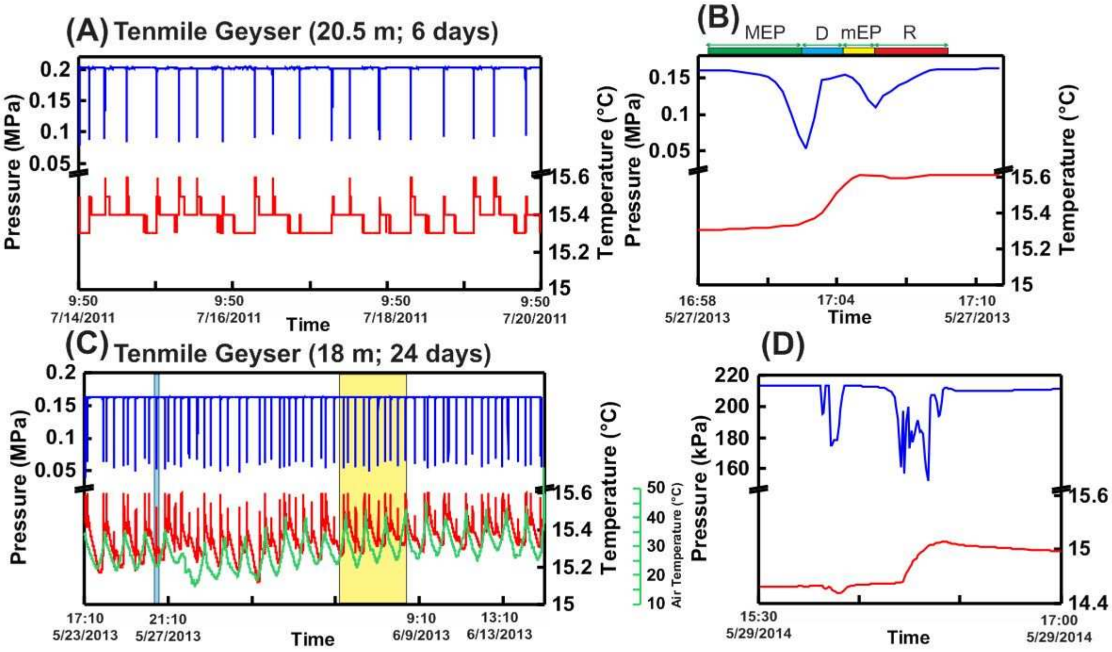

Figure 5. Periodicity of Tenmile geyser. Variations of pressure and temperature within the well of Tenmile geyser in (A) 2011 and (C) 2013, respectively. Air temperature at the nearby Crystal geyser is shown in green in (C). (B) Variations of pressure and temperature during a single eruption cycle from the blue-highlighted region in (C). The green, blue, red and yellow bars bracket the times of the MEP, D, mEP and R, respectively. (D) The pressure and temperature recorded during one of the “odd” eruptions.

4.2. Tenmile Geyser: Measurements made in 2011, 2013 and 2014

In total, 18, 62 and 29 eruptions were recorded in 2011, 2013 and 2014, respectively (Fig. 5A and C, 2014 is not shown). Tenmile geyser has a 4-part eruption cycle (Fig. 5B) which has a relatively consistent eruption length of 11.2±0.67 minutes. The interval between eruptions is comparatively more variable, averaging 8.5±2.6 hours (minimum and maximum intervals were 4.2 and 18 hours, respectively) (Fig. 4B). Increased bubbling of CO_2 from the well initiates the initial MEP (Fig. 5B) emitting jets up to 2-3 m high (Fig. 6) for ~2 minutes. Then the eruption suddenly ceases and water rapidly drains back into the well (D in Fig. 5B). After D, the water level begins to rise accompanied by vigorous CO_2 bubbling. During this time, ascending $CO_{2(g)}$ and liquid water only reach the casing top (1 m). The mEP ends with bubbling ceasing and water remaining at surface elevation, slowly rising until the next eruption (R in Fig. 5B).

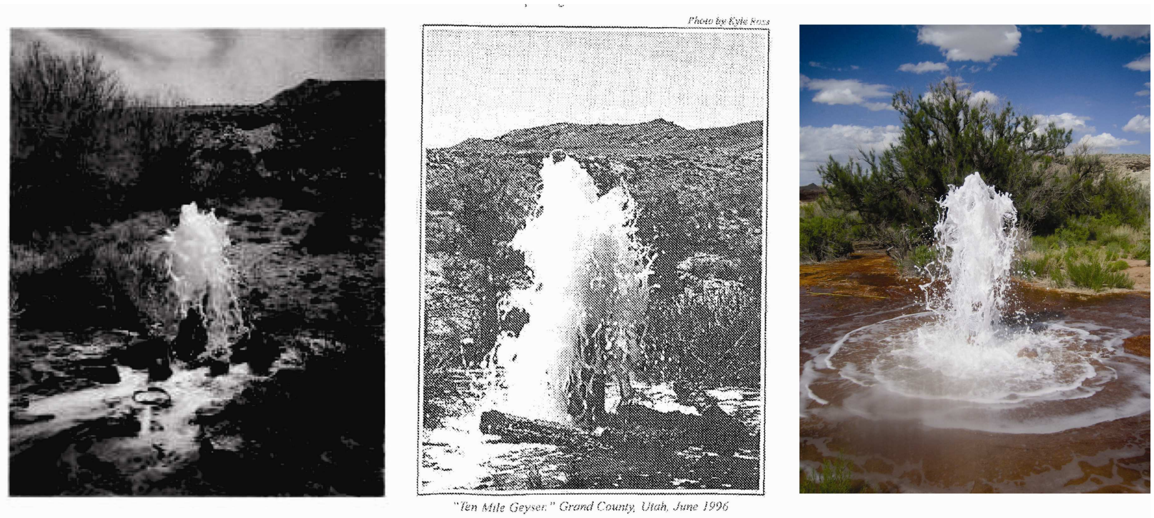

Doelling (1994)

Ross (1997)

This Study (2013)

Figure 6. Photos of eruptions at Tenmile geyser in 1994, 1997 and 2013. The photos highlight the consistency of the eruption heights at Tenmile geyser throughout its history.

In the summer of 2014 Tenmile geyser was instrumented with a suite of 4 transducers at depths of 3.5, 8.2, 12.6 and 19.7 m below the surface. The recorded variations in temperature during an eruption revealed that these changes are primarily a function of the atmospheric temperature and not the eruption itself. As seen in Fig. 7C, when the air temperature (30 ºC) is much greater than the in-well fluid temperature (15 ºC), an increase of 0.8 ºC is seen at 3.5 m. Conversely, when the air temperature (7 ºC) is lower than the in-well fluid temperature (14.5 ºC, Fig. 7A), a decrease of 0.3 ºC is observed at a 3.5 m depth.

Additionally the degree of temperature change decreases with increasing depth (Fig. 7). This phenomenon is explained in a manner similar to the mEP at Crystal geyser. Following an eruption period the water level slowly rises and pools around the well at the surface. Over the course of ~8.5 hours the pooled water temperature is affected by the ambient air and ground temperature. Then during the drainage period (D) this pooled water reenters the well and its temperature is recorded by the transducers. Thus the best reference to the temperature change caused solely by the eruption is observed at the greatest depth (19.7 m) where temperature consistently increases a relatively negligible 0.1 ºC. Other than the correlation between atmospheric and fluid temperature, no correlations exist between Tenmile geyser periodicity and external forces.

Instrumentation in 2014 revealed three eruptions much different to the typical eruption periodicity seen in other years. Fig. 5D shows the pressure recorded during one of these “odd” eruptions which the author was lucky enough to witness and record video for the entirety of the period. The eruption started normally with increased degassing building into a large eruption. Then a quiet period initiated without the drainage period which typically follows the MEP. Then the geyser began to erupt vigorously again lasting for ~10 minutes. Due to the much larger volume of water discharged during this eruption, the water level following the eruption was below the surface. The cause for these “odd” eruptions is unknown.

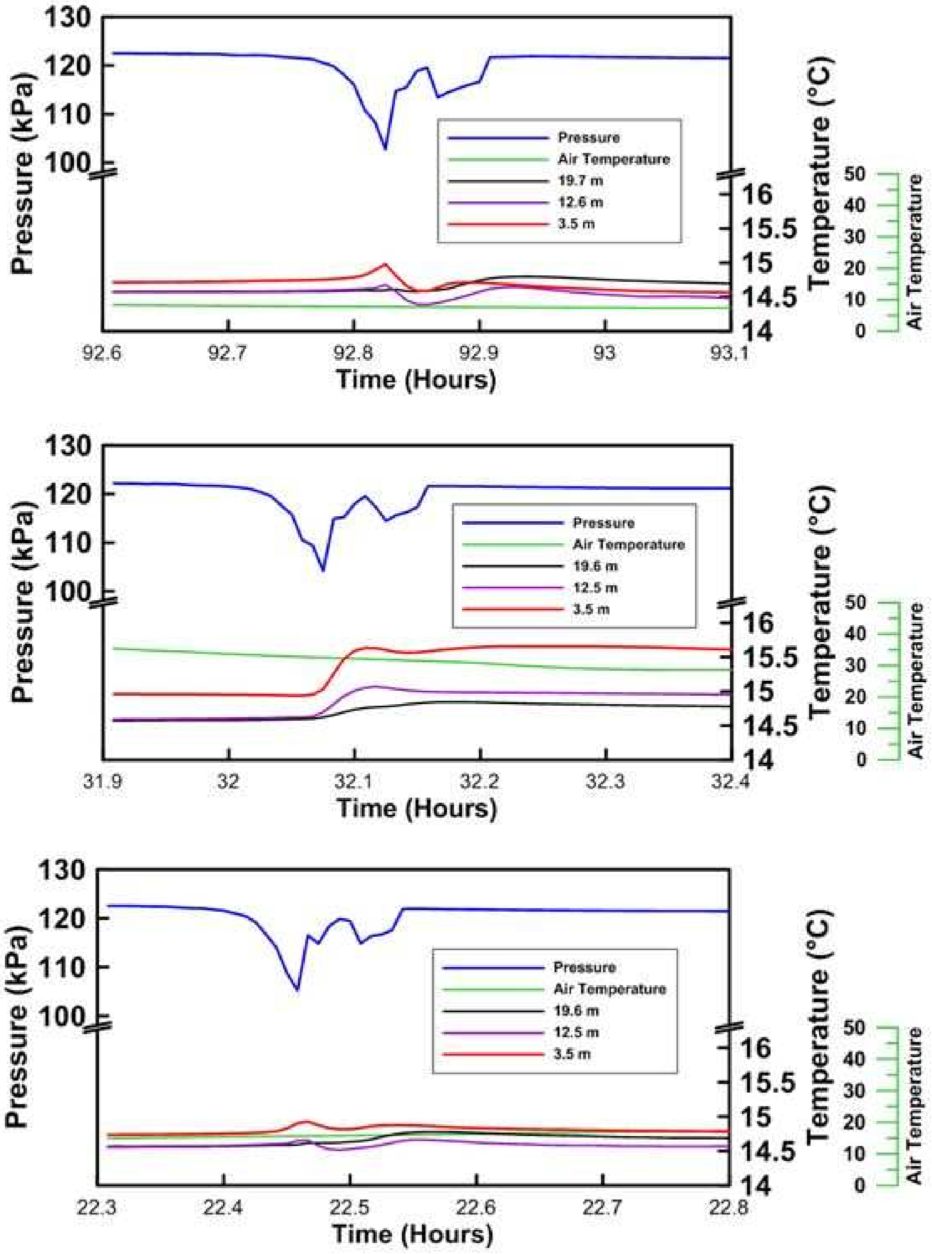

Figure 7. Pressure (blue) and fluid temperature at 3.5 m (red), 12.6 m (purple), 19.7 m (black) in comparison to air temperature (green). (A) When air temperature is lower than the mean fluid temperature, (B) when the air temperature is close to the mean fluid temperature and (C) when the air temperature is higher than the mean fluid temperature.

4.3. Chimayó Geyser: Measurements made in 2008

Chimayó geyser has a simple 2-part eruption cycle consisting of an MEP and long recharge period (Fig. 8A and B). Eruption duration averages 7.8±1.2 minutes (Fig. 4B) with plumes reaching a maximum height of 20 m. The eruption heights are greatest for this geyser predominately due to its small cross sectional area (78.5 cm^2) which drives preferential vertical volume expansion and further upward acceleration. Furthermore the water supply is limited due to the well casing which causes a more gas-dominated eruption. The mean recharge length and interval separating eruptions are 10.9±1.2 hours and 20.4±5.6 hours, respectively (Fig. 4B). Minor temperature decreases of ~0.1ºC occur during the eruption and are followed by a 0.7 ºC increase over the course of recharge. No correlations exist between Chimayó geyser periodicity and external forces.

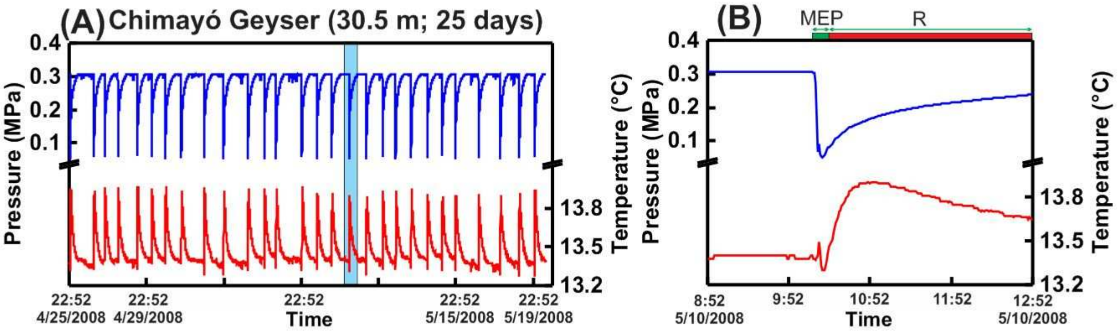

Figure 8. Periodicity of Chimayó geyser. (A) Variations of pressure and temperature within the well of Chimayó geyser in 2008. (B) Variations of pressure and temperature during a single eruption cycle from the blue highlighted region in (A). The green and red bars bracket the times of the major eruption period (MEP) and recharge (R), respectively.

5. Methodology and Analyses

The eruption mechanism of a CO_2-driven geyser is a strongly positive feedback system; CO_2 exsolution, pressure decrease, bubble growth, and buoyant migration are all interconnected parts of the eruption process (Lu et al., 2005; Zhang, 1996). The current study will determine the bubble volume fraction, flash depth, flow rate during eruptions and the eruption/annual CO_2 emission at each geyser.

5.1. Bubble Volume Fraction

As $CO_{2(aq)}$ exsolves, it begins a buoyant ascent as bubbles grow. Gas occupation increases towards the surface from the flash point within the wellbore. The fractional occupation of $CO_{2(g)}$ in brine (α) is predicted from *in situ* temporal pressure and temperature data measured by two transducers at different depths (Lu et al., 2005).

$$\alpha = 1 - \frac{\rho_m}{\rho_l} . \ (1)$$

$$\rho_m = \frac{P_1 - P_2}{gh} . \ (2)$$

Where α is the bubble volume fraction, ρ_m is the mean mixture ($CO_{2(g)}$ and brine) density, and ρ_l is the brine (H_2O-NaCl) density. ρ_m is determined by the pressure difference over depth where P is pressure ($P_1 > P_2$), g is gravitational acceleration, and h is the distance between two transducers. For example, the α obtained from Chimayó geyser refers to the bubble volume fraction between transducers at depths of 30.5 and 32

m. ρ_l was calculated with the algorithm by Batzle and Wang (1992) using the measured concentration of NaCl in 2010; the NaCl molality was 0.1, 0.17 and 0.03 for Crystal, Tenmile and Chimayó geysers, respectively.

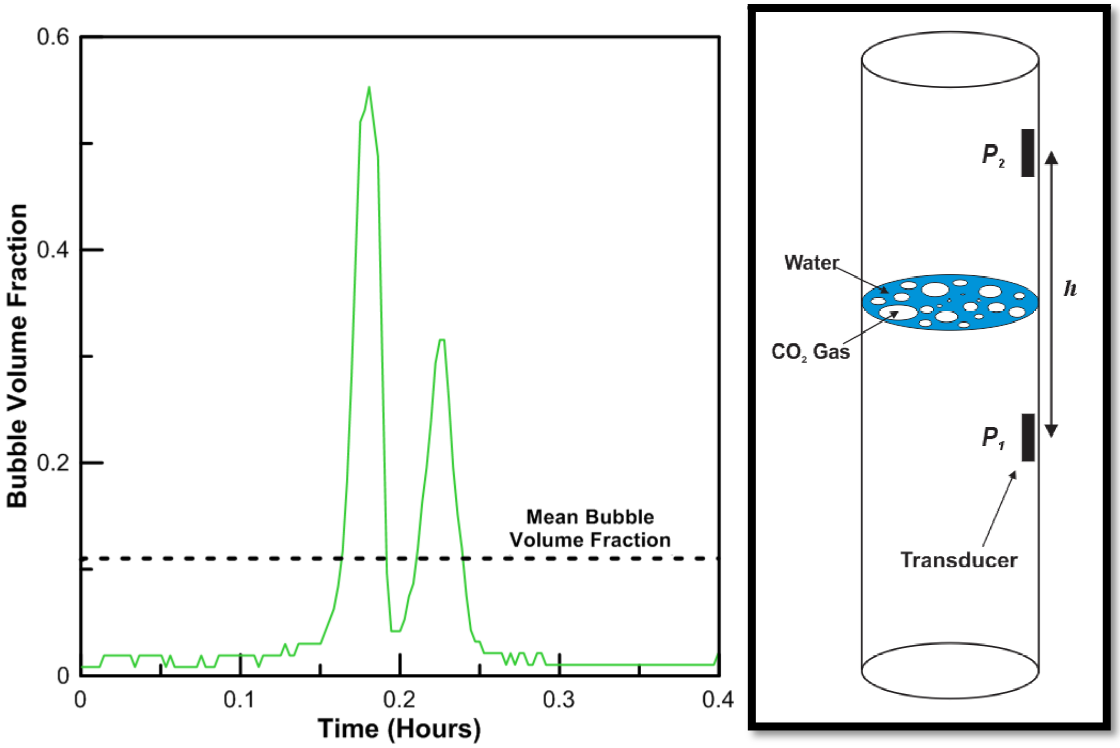

Figure 9. The evolution of bubble volume fraction over the course of an eruption at Tenmile geyser (left) and how bubble volume fraction is determined from transducer installation within a well (right).

Figure 9 shows how the bubble volume fraction is determined in the well and the bubble volume fraction during an eruption at Tenmile geyser. The calculated mean and ranges of α are listed in Table 2. The transition from diffuse bubbling to Taylor bubbles or gas slugs occurs at $\alpha \approx 0.25\text{-}0.28$ (Lu et al., 2005). Taylor bubbles or slugs are bullet shaped bubbles that occupy the entire cross sectional area of the well. Bubble volume fraction (α) values greater than 0.25, and hence the formation of slugs, produces vigorous eruptions. Crystal geyser's mEP(A) and mEP(C) α was 0.11 between two transducers (6.5 m and 14 m), suggesting that the formation of slugs is above these depths. The MEP(B) and MEP(D) reached a maximum α of 0.70 with both averaging 0.22 throughout the eruption period; therefore slugs predominately form between transducers. Tenmile geyser has a peak α of 0.64 and a mean of 0.11 (11.5 and 20.5 m). Chimayó geyser (30.5 m and 32 m) can reach α to be 0.75 with a mean eruption value of 0.52. It is interpreted that the wells with small cross sectional area (Tenmile: 415 cm^2 and Chimayó: 78.5 cm^2) prevent horizontal expansion of the emitting $CO_{2(g)}$, and thus, allow relatively small amounts of $CO_{2(g)}$ to occupy the well rapidly and enhance vertical acceleration.

Table 2. CO_2 Emission variables and results.

	Eruption height (m): Mean (Min.-Max)	**Well Area (m^2)**	**Bubble Volume Fraction: Mean (Min.-Max)**	**Exit velocity (m/s): Mean (Min.-Max)**	**Eruption duration (min): Mean**	**CO_2 emission per eruption period (kg)**	**Annual CO_2 emission (tonnes)**
Crystal mEP(A/C)	1 (0.5-2)	0.119	0.11 (0-0.16)	4.4 (3.2-6.2)	9	$(1.02 \pm 0.42) \times 10^2$	$(8.05 \pm 3.31) \times 10^2$
Crystal MEP(B)	5 (2-8)	0.119	0.22 (0-0.70)	10 (6-12.5)	72	$(3.08 \pm 1.23) \times 10^3$	$(6.75 \pm 2.70) \times 10^2$
Crystal MEP(D)	5 (2-8)	0.119	0.22 (0-0.73)	10 (6-12.5)	348	$(1.50 \pm 0.60) \times 10^4$	$(3.29 \pm 1.32) \times 10^3$
Tenmile	2 (1-3)	0.042	0.11 (0-0.64)	6.25 (4.5-8)	10.75	$(5.63 \pm 1.58) \times 10^1$	$(6.17 \pm 1.73) \times 10^1$
Chimayó	18 (16-20)	0.008	0.52 (0-0.75)	18.5 (17-20)	8.5	$(1.58 \pm 0.14) \times 10^2$	$(6.54 \pm 0.57) \times 10^1$

5.2. Eruption Velocity

The change in enthalpy over a given depth has been used to determine the eruption velocity for hot water geysers and volcanoes (Karlstrom et al., 2013; Kieffer, 1989; Mastin, 1995). Even if temperature plays a large role in the solubility of CO_2 in water, the small change in observed temperature over depth at each of the geysers infers that it plays a minor role for the CO_2 degassing process during an eruption cycle (i.e. pressure change plays a much larger role). In this work, assuming that the CO_2 flow is compressible and soluble, Bernoulli's equation is most suitable for determining eruption velocities of CO_2-driven geysers. Assuming the Ostwald solubility coefficient of CO_2 (λ) is roughly independent of pressure, Zhang (1996) derived the equation of state for CO_2-liquid water mixtures ($\rho_f / \rho \approx 1 + \lambda P_f / P - \lambda$). Furthermore, using Bernoulli's equation (eq. 3), Zhang (1996) predicted the erupting fluid velocity caused by degassing of CO_2-saturated lake bottom waters at Lake Nyos.

$$\int_{P_f}^{P_i} \frac{dP}{\rho} + \int_{\upsilon_f}^{\upsilon_i=0} \upsilon d\upsilon + \int_{z_f}^{z_i} g dh = 0 \,. \quad (3)$$

Where P is pressure, ρ is the liquid density, υ is the eruption velocity, g is gravitational acceleration, and h is a subsurface depth. Subscript *i* and *f* indicate the flash depth and surface conditions, respectively. The pressure gradient for application in Eq. 3 was developed by using the mean value over the eruption period. Fig. 10A shows the input parameters of temperature and pressure over depth. The temperature gradient for Crystal and Tenmile geysers (21.2 ºC/km) was obtained from Heath et al. (2009) and the recorded temperature gradient (36 ºC/km) between transducers was used for Chimayó geyser. The solubility of CO_2, shown in Fig. 10B, was determined based upon the concentration of NaCl, mean pressure and temperature during eruptions using the algorithms developed by Duan and Sun (2003). The density profile of the NaCl-CO_2-H_2O fluid shown in Fig. 10B was determined using Duan et al. (2008).

Table 3. Fluid density as a function of pressure where ρ is the density of the NaCl-CO_2-H_2O fluid in kg/m^3 and P is pressure in Pascals.

Eruption	Fluid Density Equation
Crystal Geyser mEP(A/C)	$\rho(P) = -6\times10^{-13}P^2 + 5\times10^{-6}P + 1003.1$
Crystal Geyser MEP(B/D)	$\rho(P) = -7\times10^{-13}P^2 + 5\times10^{-6}P + 1003.2$
Tenmile Geyser	$\rho(P) = -7\times10^{-13}P^2 + 5\times10^{-6}P + 1006.5$
Chimayó Geyser	$\rho(P) = -2\times10^{-12}P^2 + 5\times10^{-6}P + 1000.9$

A second order polynomial equation showing the functional relationship between the density and pressure of each geyser is shown in Table 3 for use in Eq. 3. By solving Eq. 3 with the predicted mixture density (ρ) profiles, the relationship between eruption velocity ($\square_f$) at the surface and the depth (h) at which an eruption initiates was determined (Fig. 10C). The eruption velocity of each geyser is predicted from a visual estimate of eruption height (H) and the ballistic equation ($\upsilon_f = \sqrt{2gH}$). Karlstrom et al. (2013) utilized particle image velocimetry (PIV) along with the ballistic equation to determine the eruption velocity at Lone Star geyser, Yellowstone National Park. Comparison of these methods suggested that PIV and ballistic methods provided upper and lower bounds for the exit velocity, respectively. Only when the eruption was steam dominated did the ballistic equation overestimate the velocity. Such gas dominated eruption periods do not exist for the geysers studied here. Finally, the flash depth (h) was predicted by constraining the exit velocity with the observed minimum and maximum eruption height (H); the observed H is shown in Table 2.

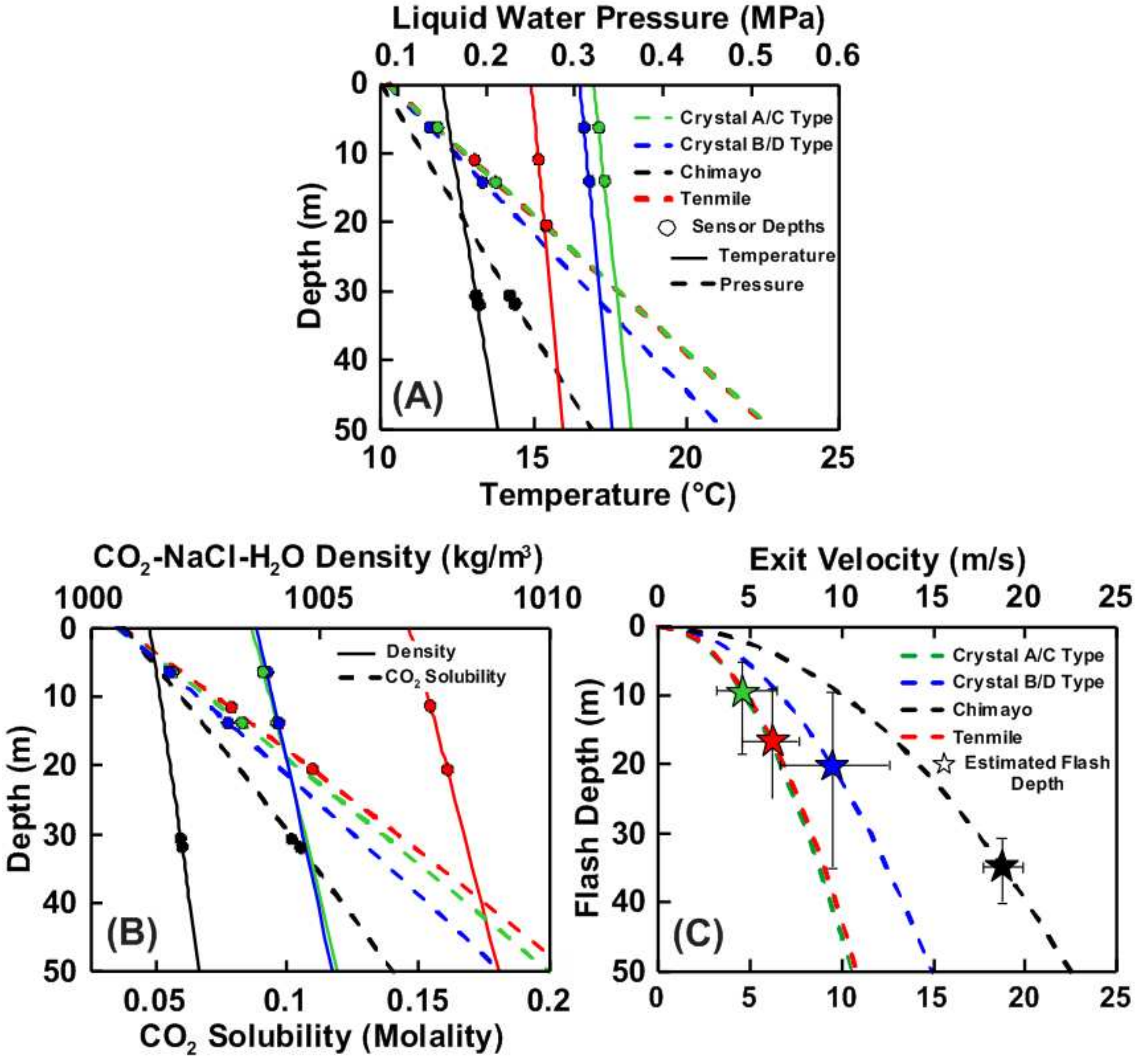

Figure 10. (A) Interpolated eruption pressure (dashed lines) and temperature gradients (solid lines) based on the measured pressure and temperature at two transducers. (B) CO_2 solubility profiles (dashed lines) calculated from Duan and Sun (2003) and density of the CO_2-NaCl-H_2O mixture (solid lines) over depth calculated from Duan et al. (2008). (C) Calculated relationship between exit velocity and

flash depth. Stars and error bars represent predicted flash depths of Crystal, Tenmile, and Chimayó geysers.

Estimates and ranges of the flash depth are shown in Fig. 11C. The mEP(A/C) at Crystal geyser reach mean heights of 1 m with a υ of 4.4 m/s, revealing that eruptions initiate, on average, 9 m below the surface. Maximum eruption heights of 8 m occur during the MEP(B/D) equating to a maximum υ of 12.5 m/s. In most cases, eruptions predominately reach heights of 2-5 m with a corresponding υ of 6-10 m/s. Therefore the flash depth has a wide range (10 to 35 m) but typically initiates around a 20 m depth. The eruptions at Tenmile geyser reach a maximum height of 3 m resulting in a υ of 7.7 m/s. The flash depth required to produce plumes that height would be 25 m below the surface while the mild eruption could initiate at 9 m. The eruptions at Chimayó geyser (16-20 m) initiate at a depth 31 to 40 m below the surface. We expect that imperfections in conduit geometry, fractures enhancing lateral expansion of $CO_{2(g)}$ and friction caused by well-filling rocks (except Chimayó geyser, which is cased with PVC) could cause an error in the estimation of the velocity over depth and, subsequently, the estimation of flash depth.

5.3. Mass Emission

Using the mean bubble volume fraction, eruption velocity and eruption period, the mass of $CO_{2(g)}$ emitted was determined with eq. 4.

$$m_{CO_2} = (\alpha A_w)\rho\upsilon\Delta t \,. \quad (4)$$

where m_{CO_2} is the mass of CO_2, α is the mean bubble volume fraction, υ is mean eruption velocity, ρ is the density of $CO_{2(g)}$, A_w is the cross sectional area of the well and Δt is the mean time length of the eruption. Thus the equation is set to determine the net mass of $CO_{2(g)}$ that has passed between transducers and does not account for CO_2 exsolution shallower than this point. The density (ρ) of $CO_{2(g)}$ flowing through the measurement point (mid-point between transducers) was determined from the mean pressure and temperature during an eruption using Span and Wagner (1996). The times used are the mean eruption length (Δt); annual estimates are made with the subsequent mean amount of eruptions per year. The estimate for Crystal geyser is based on the eruption data recorded in 2010. As a whole, all eruptions from Crystal geyser are estimated to emit $(4.77\pm1.92)\times10^3$ tonnes annually. The annual CO_2 emission determined by Gouveia et al. (2005) was 1.1×10^4 tonnes where they used a down-wind grid of Gray box samplers to measure the CO_2 concentration in the air. The estimate of CO_2 discharge rate during single minor eruptions are very similar at 1.7×10^{-1} kg/s and 1.9×10^{-1} kg/s for Gouveia et al. (2005) and this study, respectively (minor eruptions were referred to as “pre-eruptive events” in Gouveia et al. (2005)). The primary discrepancy between annual estimates is likely explained by the increase in eruption interval since the measurements by Gouveia and Friedmann (2006) (Fig. 4A) and that CO_2 detected by their instruments will have come not only from the geyser but surrounding springs and diffuse flux from the ground. As revealed by Burnside et al. (2013) and Jung et al. (2014), significant amounts of diffuse CO_2 gas leaks through the Little Grand Wash fault traces. For example, Jung et al. (2014) measured $CO_{2(g)}$ flux of 36 kg/m^2/day adjacent to Crystal geyser in 2013 which would accumulate in 1.3×10^4 kg/m^2/yr. Furthermore, the growing blockages within the well presumably act in a manner to retard bubble growth and acceleration, diminishing the net release of $CO_{2(g)}$. Thus this estimate of CO_2 emitted is more accurate of Crystal geyser's present state. Tenmile and Chimayó geysers emit $(5.63\pm1.58)\times10^1$ kg and $(1.58\pm0.14)\times10^2$ kg of CO_2 for an eruption accumulating in $(6.17\pm1.73)\times10^1$ tonnes and $(6.54\pm0.57)\times10^1$ tonnes annually, respectively. The reason for much higher estimates at Crystal geyser is that it not only discharges greater volumes of CO_2 per eruption but also the ratio of eruptive time to quiet time (Crystal: 0.33, Tenmile: 0.02, and Chimayó: 0.01) is 17-50 times larger (Fig. 4A).

6. Periodic changes in Effluent Chemistry

Determining the mechanisms which cause the periodic eruptions from geothermal and CO_2-driven geysers has been a common objective among researchers in the field (Belousov et al., 2013; Gouveia and Friedmann, 2006; Han et al., 2013; Hurwitz et al., 2012; Hurwitz et al., 2014; Ingebritsen and Rojstaczer, 1993; Karlstrom et al., 2013; Kieffer, 1989; Lu et al., 2006; Vandemeulebrouck et al., 2013; Watson et al., 2014). Investigations with various tools such as in-geyser video observations, water sampling and numerical modeling have provided a great deal of insights into the operations of geysers. Utilizing a suite of temporal water sample datasets from multiple field trips to Crystal geyser, systematic and repeated trends in effluent water chemistry have been revealed. Crystal geyser is the only known geyser which exhibits these repeating dramatic changes in water chemistry that coincide with its unique eruption cycle. The chemical characteristics of the water suggest that the sources for Crystal geyser vary throughout the eruption cycle. Inverse modeling utilizing fluid endmembers is conducted to determine the fractional contribution from multiple sources during each eruption period revealing new insights into the subsurface dynamics which govern the eruptions at Crystal geyser.

7. Sampling Methods

Between 2007 and 2014 the CO_2-driven cold-water springs and geysers of the Green River, Utah region (Fig. 1A) were monitored and sampled for their water chemistry. All water samples collected from Crystal geyser were obtained through the hole at the base of the casing (Fig. 1C) to prevent sampling the surrounding pool water. Details of fluid sampling in October 2007 and September 2010 (2010a) can be found in Kampman et al. (2009) and Kampman et al. (2014), respectively. Water samples collected in December 2010 (2010b), May 2013 and 2014 samples were filtered through a 0.2 μm filter. 2010b samples were acidified in the field and sent to Los Alamos National Laboratory for cation analysis. Anions were analyzed at the University of Utah. The May 2013 samples were analyzed using ion chromatography and atomic absorption for anions and cations, respectively, at the University of Wisconsin-Milwaukee. None of the May 2013 samples were acidified preventing analysis of elements like Ca^{2+}, Mg^{2+} and SO_4^{2-}. ^{18}O and D isotopes were analyzed using a Picarro L2130-I at the University of Wisconsin-Milwaukee. May 2014 samples were collected in a similar fashion as the 2013 samples. Cations were analyzed at Los Alamos National Laboratory. Anions were analyzed using ion chromatography at the University of Wisconsin-Milwaukee. pH measurements and alkalinity end-point titrations were made immediately after sampling in the field. In situ monitoring of pH, dissolved oxygen and electrical conductivity was conducted in 2013 and 2014 using a Hydrolab MS5. pH measurements have an accuracy and resolution of ± 0.2 units and 0.01 units, respectively. Dissolved oxygen measurements have an accuracy and resolution of ± 0.2 mg/L and 0.01 mg/L, respectively. Electrical conductivity measurements have an accuracy and resolution of ± 1 µS/cm and 1×10^{-4} units, respectively.

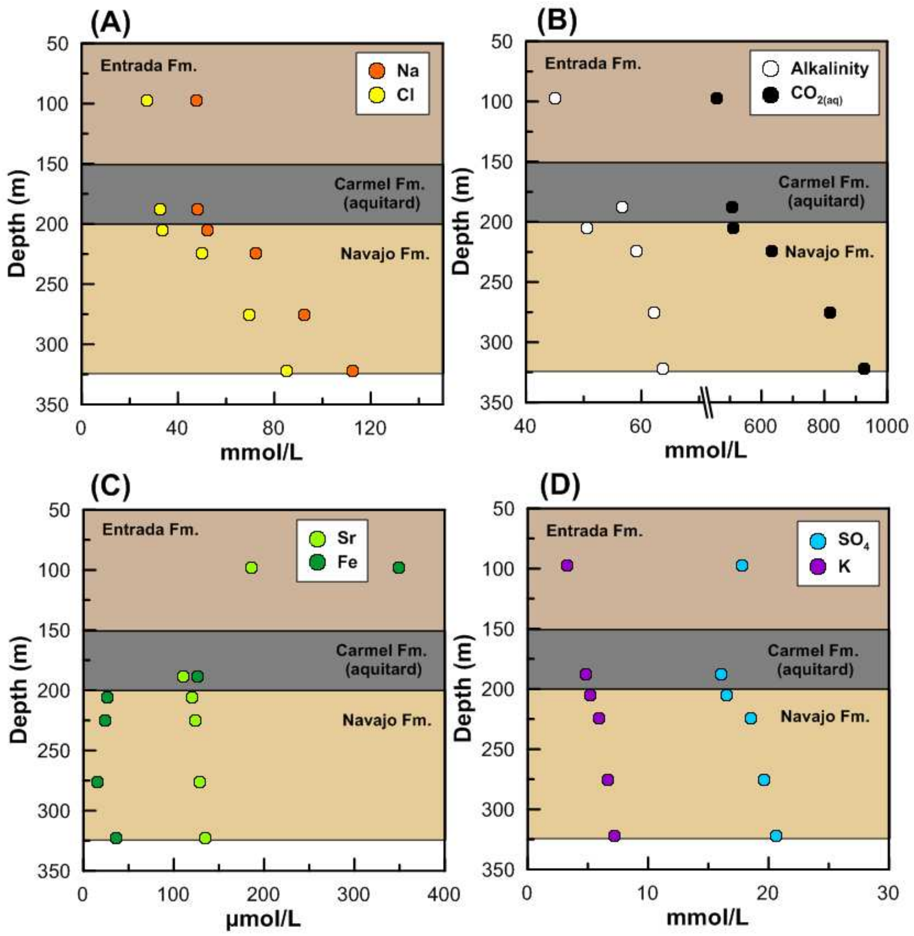

Figure 11. Chemical speciation within the Entrada, Carmel and Navajo Formations near Crystal geyser from Kampman et al. (2014). (A) Concentration of Na (orange circle) and Cl (yellow circle) in mmol/L. (B) Concentration of $CO_{2(aq)}$ (black circle) and alkalinity (white circle) in mmol/L. (C) Concentration of Sr (light green circle) and Fe (dark green circle) in μmol/L. (D) Concentration of SO_4 (light blue circle) and K (purple circle) in mmol/L.

8. Chemical and Isotopic Composition

8.1 Groundwater

Extensive characterization of the groundwater flow regime and chemical characteristics can be found in Hood and Patterson (1984) and Kampman et al. (2014), respectively. The drilling project, CO2W55, adjacent to Crystal geyser by Kampman et al. (2014) provided a significant insight in the chemical speciation within the aquifers that supply Crystal geyser. These aquifers are the Entrada Sandstone (0-150 mbs) and the deeper Navajo Sandstone (206-322 mbs), separated by the impermeable Carmel Formation (150-206 mbs). Both downhole and open-hole samples were collected where downhole (sampled in situ) samples are more accurate of the chemical speciation at the specific depth. Open-hole samples will experience some contamination as they migrate upwards and mix with other fluids over depth. Thus only the downhole samples are shown here unless noted otherwise. Progressive enrichment in brine-typical elements, Na^+, K^+, Cl^- and SO_4^{2-}, are witnessed towards the base of the Navajo Sandstone (Fig. 11A and 11D). Additionally, increasing CO_2 saturation, decreasing pH and increased alkalinity highlight the coupled nature of brine and CO_2 as they migrate up along the Little Grand Wash (LGW) fault. The increasing concentrations over depth in the Navajo may be explained by the fluid density differences between CO_2-brine and meteoric water in addition to the fluids originating from depth. The molar abundance of the major cations and anions within the groundwater systems follow $Na^+ > Ca^{2+} > Mg^{2+} > K^+$ and $Cl^- > HCO_3^- > SO_4^2$, respectively. Significantly greater concentrations of Fe^{2+} and Sr^{2+} are seen in the Entrada Sandstone compared to the Navajo Sandstone (Fig. 11C).

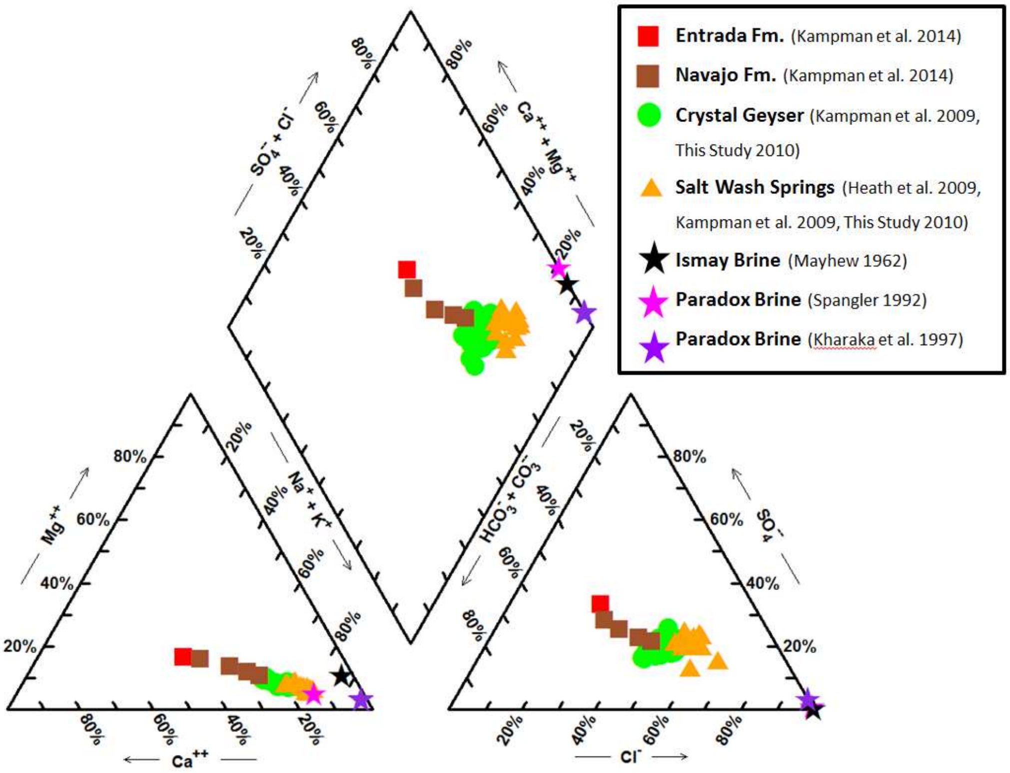

Figure 12. A Piper plot of the Entrada Sandstone (red square), Navajo Sandstone (brown square), Crystal geyser in 2007 (green circle) and the Salt Wash Springs (orange triangle), Ismay Brine (black star) and the Paradox Brine (pink and purple stars).

Considerable variation in $\delta^{18}O$ and δD occurs over depth. $\delta^{18}O$ and δD vary from -13.09 to -15.63 ± 0.2 ‰ and -110.1 to -118.2 ± 1.0 ‰, respectively. As seen in Fig. 13, these samples deviate from the North American Meteoric Water Line (NAMWL) towards a heavier concentration. The relatively normal geothermal gradient of 21.2 □C/km infers that excessive heating of groundwater cannot be the cause of this isotopic enrichment (Heath et al., 2009). Additionally, it is unlikely that significant changes in elevation during recharge could explain these isotopic variances or enrichments. The isotopic signature of the Ismay Brine from the Paradox Fm. is 42.0, 2.2, matching well with the observed deviation of the groundwater samples (Spangler, 1992). Surprisingly, since CO_2 and brine seemingly migrate together within the system, the heaviest isotopic signature is seen within the shallow Entrada Sandstone (Fig. 13).

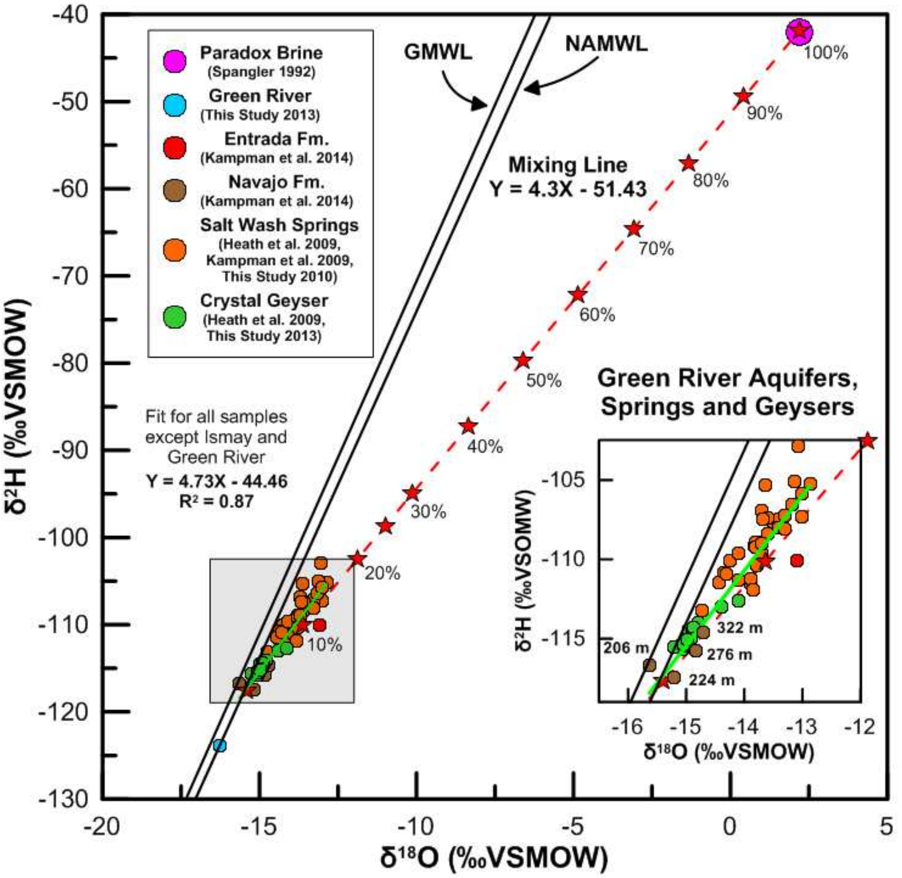

Figure 13. δD and $\delta^{18}O$ values for the Ismay Brine (pink circle), Salt Wash Springs (orange circle), Entrada and Navajo Sandstones (red and brown circles, respectively), Crystal geyser (green circle) and the Green River (light blue circle). An interpolated trend line (red dashed line) is shown between the Springs, Geysers and Aquifers to the Ismay Brine. A trend line for just the Springs, Geysers and Aquifers is shown (solid green line). The inset provides a closer view of the positions of the samples. Additionally, the depth of the Navajo samples are shown next to their positions in the inset.

8.2 Springs and Geysers

The earliest analyses of Crystal geyser's effluent were conducted by Barton and Fuhriman (1973) and Mayo et al. (1991). A number of additional trips to sample Crystal geyser and the other CO_2-driven springs have been conducted since the early 2000's (Assayag et al., 2009; Heath et al., 2009; Kampman et al., 2009; Kampman et al., 2014). The molar abundance of the major cations is the same as the Entrada and Navajo; $Na^+ > Ca^{2+} > Mg^{2+} > K^+$. The molar abundance of the major anions follow the order of $Cl^- > HCO_3^- > SO_4^{2-}$. The majority of the CO_2-driven springs (including Tenmile geyser) lie to the south of Crystal geyser along the Salt Wash (SW) Fault where a notable increase in Na^+, K^+, Cl^- and SO_4^{2-} is seen. In general, the CO_2-driven springs and geysers share a similar chemical composition as evidenced by their positions on the Piper plot (Fig. 12). The $\delta^{18}O$ and δD values of the geysers, springs, groundwaters and Green River are shown in Fig. 13.

Crystal geyser has a range of -14.10 to -15.22 and -112.60 to -115.66 for $\delta^{18}O$ and δD, respectively (Heath et al., 2009). The Salt Wash Springs range from -12.87 to -14.74 ± 0.2‰ and -102.89 to -111.5 ± 1.0‰ (Heath et al., 2009). The springs and geysers also show a deviation from the NAMWL towards a heavier concentration with respect to $\delta^{18}O$

and δD. Consistent with the elevated concentrations of Na^+, K^+, Cl^- and SO_4^{2-} seen along the SW Fault, the SW springs and geysers (orange circles in Fig. 13) also exhibit isotopically heavier values. An inferred trend line (red dashed line in Fig. 13) was added between the NAMWL and the Ismay Brine sample showing that the input of brine varies from 0-15% for the springs, geysers and aquifers. Adding a trend line (green line in Fig. 13) without the Ismay Brine infers a slightly lighter, with respect to $\delta^{18}O$, source of brine.

8.2.1 Source of additional salts

The concentration of Na^+, K^+, Cl^- and SO_4^{2-} is greater in the effluent of the springs and geysers than the Entrada and Navajo Sandstones. Thus there must be an additional source of salts. Three potential scenarios exist which could explain the discrepancy. A. Brine may directly reach the well or conduit of the springs and geysers through fault damage zones or fracture networks. Fracture networks encountered throughout the drilling project adjacent to Crystal geyser highlight the high probability of Crystal geyser penetrating its own set of fracture networks (Kampman et al., 2014). B. Crystal geyser is 45 m from the Little Grand Wash Fault and the CO2W55 well is 90 m from the fault, Crystal geyser may be sampling more brine rich fluids due its closer proximity to the fault. Or C. Crystal geyser is fed by deeper and more saline waters (Wingate Sandstone) which were not sampled during the CO2W55 drilling project. In conclusion any of these scenarios or a combination of them could explain the discrepancy between observed concentrations at depth and at the surface.

9. Temporal Variations in Effluent Chemistry at Crystal Geyser and Tenmile Geyser

Despite the extensive work on geyser dynamics, very few researchers have attempted temporal eruption cycle water sampling as an investigative tool (Hurwitz et al., 2012; Kampman et al., 2014; Noguchi and Nix, 1963). Noguchi and Nix (1963) were the very first at investigating the changes of water chemistry during eruption cycles at five geysers in Yellowstone National Park. The most significant trend noted at Old Faithful geyser was a 12% variation in the concentration of SO_4^{2-} throughout the duration of an eruption. Further investigation by Hurwitz et al. (2012) revealed less dramatic changes in effluent chemistry from Old Faithful, however the largest changes were once again, SO_4^{2-}. Kampman et al. (2014) was the first to reveal the temporal variations in effluent chemistry from the CO_2-driven cold-water geyser, Crystal geyser, in Green River, Utah. While the revelation was significant, little interpretation or analysis was made upon the results. Here we present an in depth analysis on temporal water samplings of Crystal geyser from November 2007 (Kampman et al., 2014), September 2010 (2010a) (Kampman et al., 2014), December 2010 (2010b1 and b2), May/June 2013, May/June 2014 (Appendix A).

The eruption cycle at Crystal geyser has shown considerable variation since it was drilled in 1936 (Watson et al., 2014). The eruption cycle during the sampling periods presented here were 6- and 4-part for the sampling periods in 2007-2010 and 2013-2014, respectively. While the eruption cycle has varied over time the main constituents such as the minor eruption period (mEP), major eruption period (MEP) and recharge (R) were present in the varying forms and orders for all of the sampling periods.

9.1 Hydrochemical Variations during the mEP

Just prior to the mEP, temperature rises from below 16.8 to 17.2 ºC over the course of ~10 hours. Slight oscillations in temperature occur during this period as discharged water pools around the well and is either warmed or cooled by the current atmospheric temperature (Watson et al., 2014). The mean concentration of Na^+ in 2007, 2010b1 and 2014 during the mEP was 168, 164 and 157 mmol/L, respectively (Fig. 15 and 17). The percent increase in Na^+ during the two complete sampled mEP in 2014 was 15% and 16%. K^+ saw a 9% and 10% increase during the mEP in 2014 (Fig. 17). The mean concentration of Cl^- in 2007, 2010b1 and 2014 was 126, 113 and 108 mmol/L, respectively. The percent increase in Cl^- during the mEP in 2014 was 15% and 16%. Matching well with the change in Na^+, K^+ and Cl^-, electrical conductivity begins to increase from a base value of 19,000 µS/cm at the same time as temperature increases. The rise of electrical conductivity occurs throughout the first half of the mEP and remains steady once reaching a value of 21,250 µS/cm (Fig. 14A). In situ monitoring of pH reveals oscillations of 0.05-0.15 but generally increases from 6.3 to 6.4 over the course of the mEP. During minor eruptions, pH spikes and increases due to the production of $CO_{2(g)}$ as shown in the equation below. The consumption of H^+ causes the pH of the solution to increase.

$$H^+ + HCO_3^- \xrightarrow{yields} CO_{2(g)} + H_2O$$

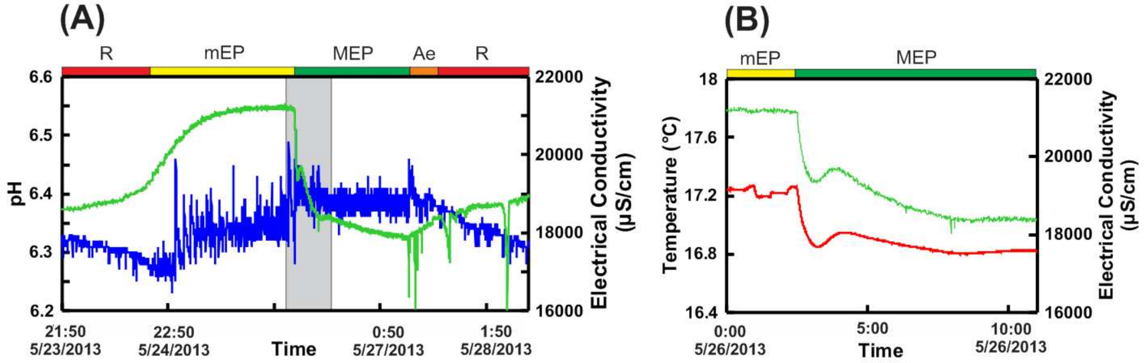

Figure 14. (A) Variations in electrical conductivity (green) and pH (blue) over the course of a single eruption cycle at Crystal geyser in May 2013. The red, yellow, green and orange bracket bars represent the R, mEP, MEP and Ae, respectively. (B) Variations in electrical conductivity (green) and temperature (red) from the grey section in 16A at the mEP/MEP transition highlighting the connection between fluid temperature and salinity.

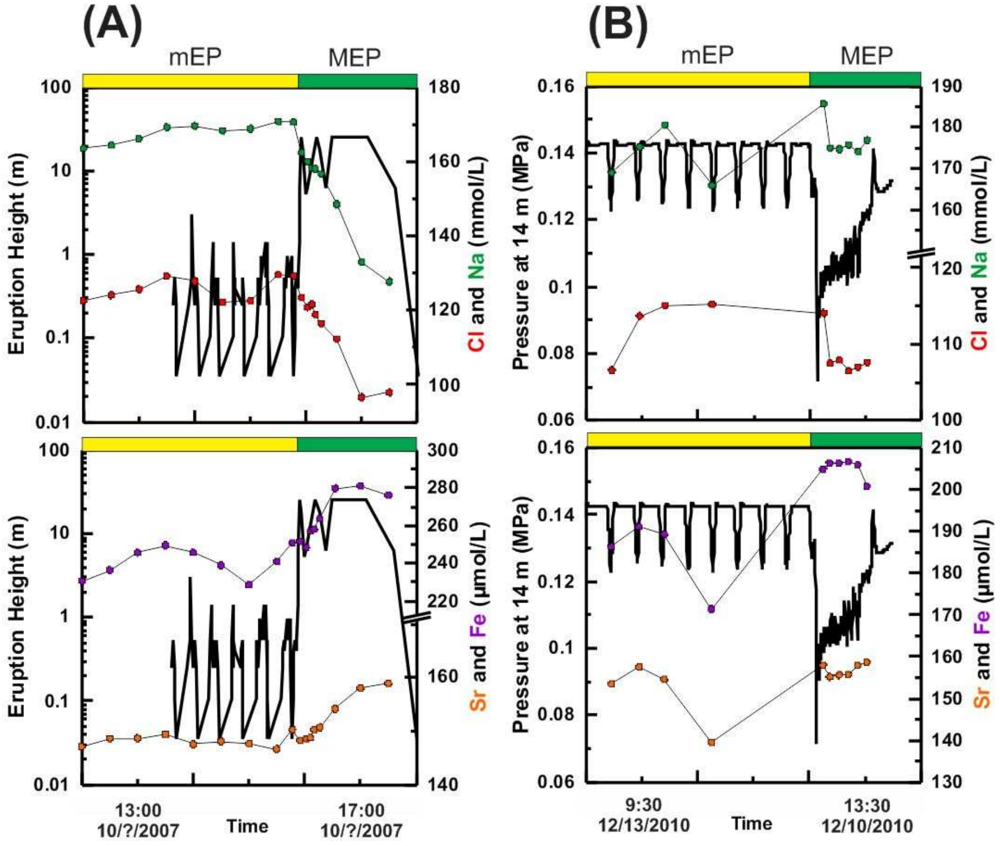

Figure 15. Variations in the concentration of Na (green circle), Cl (red circle), Sr (orange circle) and Fe (purple circle) at the mEP/MEP transition in 2007 (A) and 2010

(2010b1) (B). The eruption height and pressure is shown as a black line in (A) and (B) respectively.

9.2 Hydrochemical Variations during the MEP

At the onset of the MEP, temperature drops sharply at from 17.4 to 16.8 ºC. As revealed in section 4.1 and 4.2, the in-well fluid temperature can be affected by the current atmospheric temperature. Unlike the mEP, the MEP continually discharges water preventing the reentry of pooled water back into the well. Thus the temperature recorded by the transducers will be true to what is occurring within the well. Joule-Thomson cooling and endothermic exsolution of CO_2 was initially proposed by Han et al. (2013) as the cause of the regular 0.6 ºC decrease in temperature. Joule-Thomson cooling and exsolution of $CO_{2(g)}$ will be dependent on the evolution of bubbles along the flow path. The growing rock clog within the well will act to inhibit bubble growth and expansion. The discrepancy between a changing conduit and a consistent temperature trend suggest the temperature change is due to fluid sourcing from a shallower location and not CO_2 driven cooling. Similar to the sharp decrease in temperature, a sharp drop in electrical conductivity is seen at the onset of the MEP. Electrical conductivity decreases from its previously steady value of 21,250 μS/cm to 19,300 μS/cm and then rises slightly to 19,700 μS/cm (Fig. 14B). Following this minor rise it steadily decreases to ~18,000 μS/cm over the course of the entire MEP. Curiously, this oscillation in electrical conductivity matches perfectly with the change in temperature (Fig. 14B). It should be noted here that the recorded electrical conductivity was temperature corrected. The total change in electrical conductivity throughout the MEP is over 3,000 μS/cm, similarly the electrical conductivity of the fluid in the Navajo Sandstone has been shown to change over 3640 μS/cm from the top to the base of the formation. Not surprisingly, the concentration of Na^+ and Cl^- declines throughout the MEP. Mean concentrations of Na^+ during the MEP in 2007, 2010a, 2010b2, 2013 and 2014 were 150, 153, 151, 125 and 157 mmol/L, respectively (Fig. 15, 16 and 17). The mean concentration of Cl^- during the MEP in 2007, 2010a, 2010b2, 2013 and 2014 was 115, 122, 91, 105 and 108 mmol/L, respectively. The percent decrease in Na^+, Cl^-, K^+, Fe^{2+} and Sr^{2+} over the course of all the recorded MEP's are provided in Table 4. Smaller variations in pH (0.05) and a steady value of ~6.4 are seen for the entire period (Fig. 14). Variations in the δD and $\delta^{18}O$ values during the MEP are presented in Fig. 18.

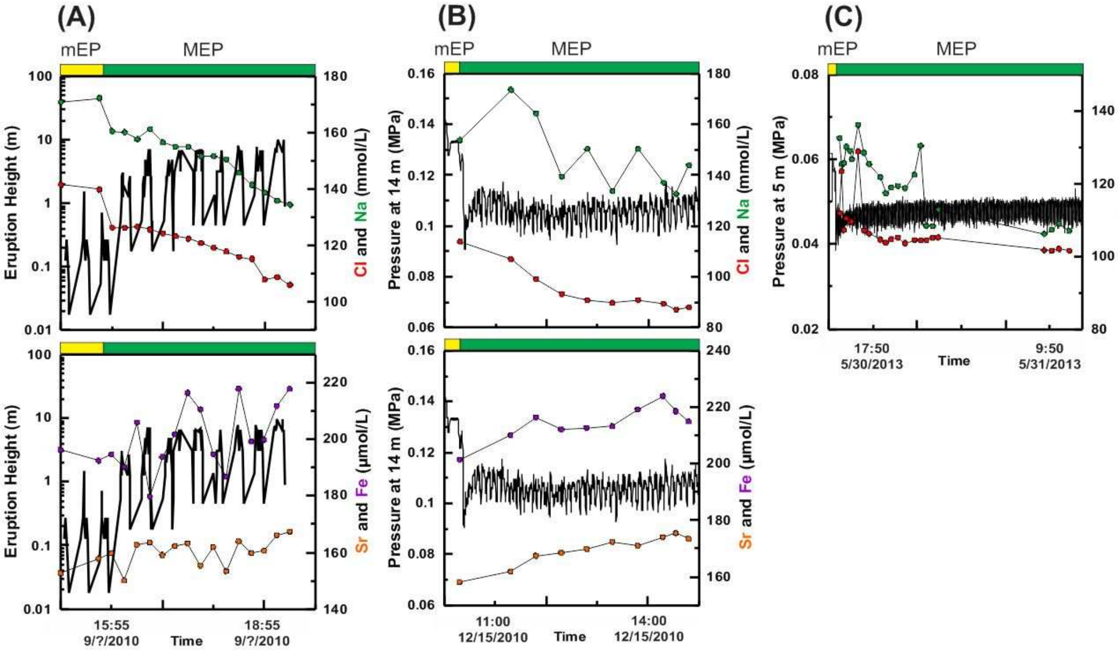

Figure 16. Variations in the concentration of Na (green circle), Cl (red circle), Sr (orange circle) and Fe (purple circle) at the mEP/MEP transition in September 2010 (A),

December 2010 (2010b2) (B) and May 2013 (C). The black line represents pressure in (B) and (C) and eruption height in (A).

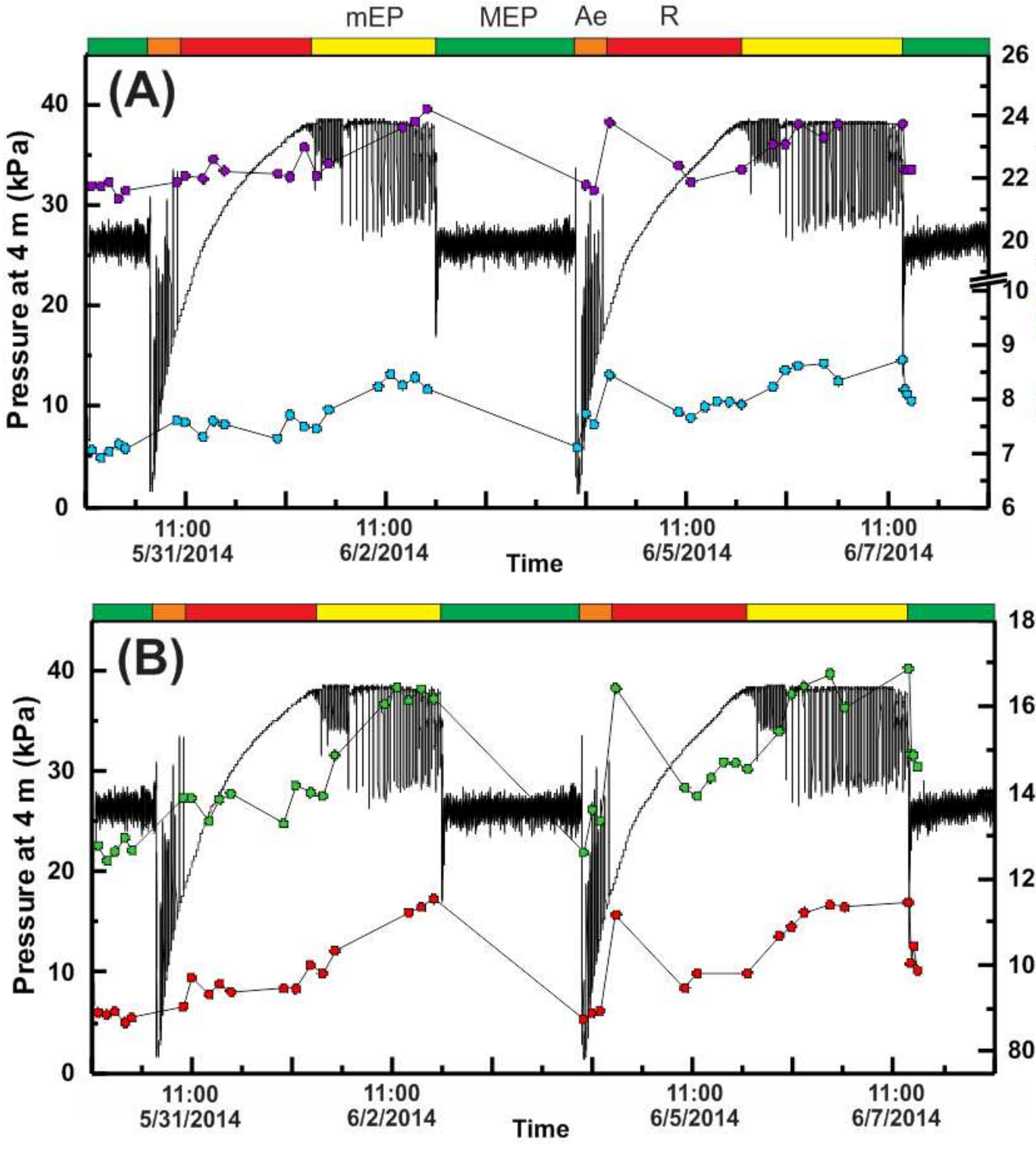

Figure 17. (A) Variations in the concentration of K (light blue circle) and SO_4 (purple circle) at Crystal Geyser in 2014. (B) Variations in Na (green circle) and Cl (red circle) in 2014. Pressure is shown in black.

9.3 Hydrochemical Variations during Recharge

During the recharge period the water level within the well continually increases from a depth of a few meters. As recharge progresses the in-well fluid temperature remains relatively steady at 16.8 ºC. Electrical conductivity begins to rise immediately as the MEP ends. Over the course of the recharge period the electrical conductivity increases roughly 1000 µS/cm from 18,000 to 19,000 µS/cm (Fig. 14A). At the same time the fluid pH progressively decreases from 6.4 to 6.25. The increasing electrical conductivity and decreasing pH further highlight the coupled nature of CO_2 and brine. During the recharge period CO_2-rich brine continue to migrate upwards. The decreasing pH can be described as seen below.

$$H_2O + CO_2 \xrightarrow{yields} H^+ + HCO_3^-$$

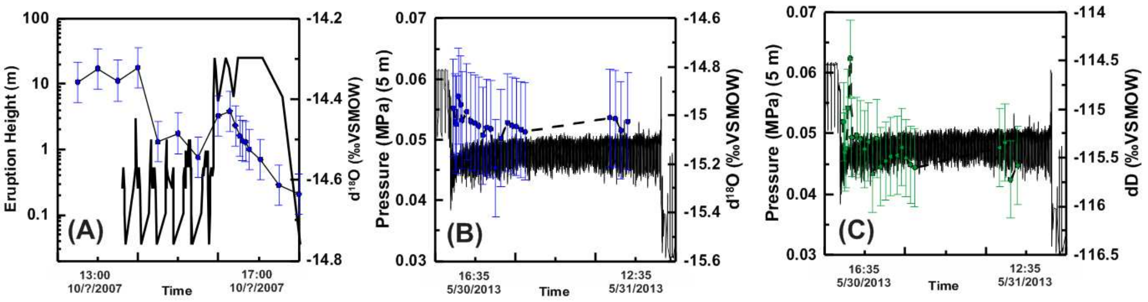

Figure 18. (A) Variations in $\delta^{18}O$ at the mEP/MEP transition at Crystal geyser in 2007. (B) Variations in $\delta^{18}O$ during the MEP at Crystal geyser in 2013 and (C) Variations in δD during the mEP at Crystal geyser in 2013.

Table 4. Percent change in ions during eruption periods. Positive and negative percentages mean increasing and decreasing concentrations, respectively. ND means No Data.

	MEP	**MEP**	**MEP**	**MEP**	**MEP**	**mEP**	**mEP**
	2007	**2010a**	**2010b1**	**2010b2**	**2013**	**2014a**	**2014b**
Na^+	-43%	-21%	-5%	-20%	-19%	15%	16%
Cl^-	-24%	-25%	-6%	-23%	-18%	15%	16%
K^+	-19%	-13%	0%	9%	ND	9%	10%
Fe^{2+}	-25%	-11%	-3%	-7%	ND	-44%	-6%
Sr^{2+}	-6%	-10%	-1%	-10%	ND	0%	-12%

9.4 Temporal trends at Tenmile Geyser

Like Crystal geyser, Tenmile geyser goes through some chemical variations during its eruption cycle, however to a much smaller degree. Prior to eruptions the electrical conductivity is relatively steady at a value of 26,250 μS/cm (Fig. 19A). During an eruption the value drops sharply towards zero due to $CO_{2(g)}$ engulfing the probes. It should be noted that the Y axis has been formatted so the minor changes in EC can be identified. Thus, the sharp drop to zero is not shown, but is inferred by the dashed lines in Fig. 19B. Once the eruption has ceased and $CO_{2(g)}$ has stopped evolving, electrical conductivity is above 26,400 μS/cm. The change in electrical conductivity is presumably due to the drawing of deeper more saline waters towards the surface. The changes in temperature during eruptions have been extensively characterized in section 4.2. Thus, the minor changes in electrical conductivity at Tenmile geyser are not necessarily to show another geyser going through its own chemical variations but more so to highlight how dramatic the changes are at Crystal geyser.

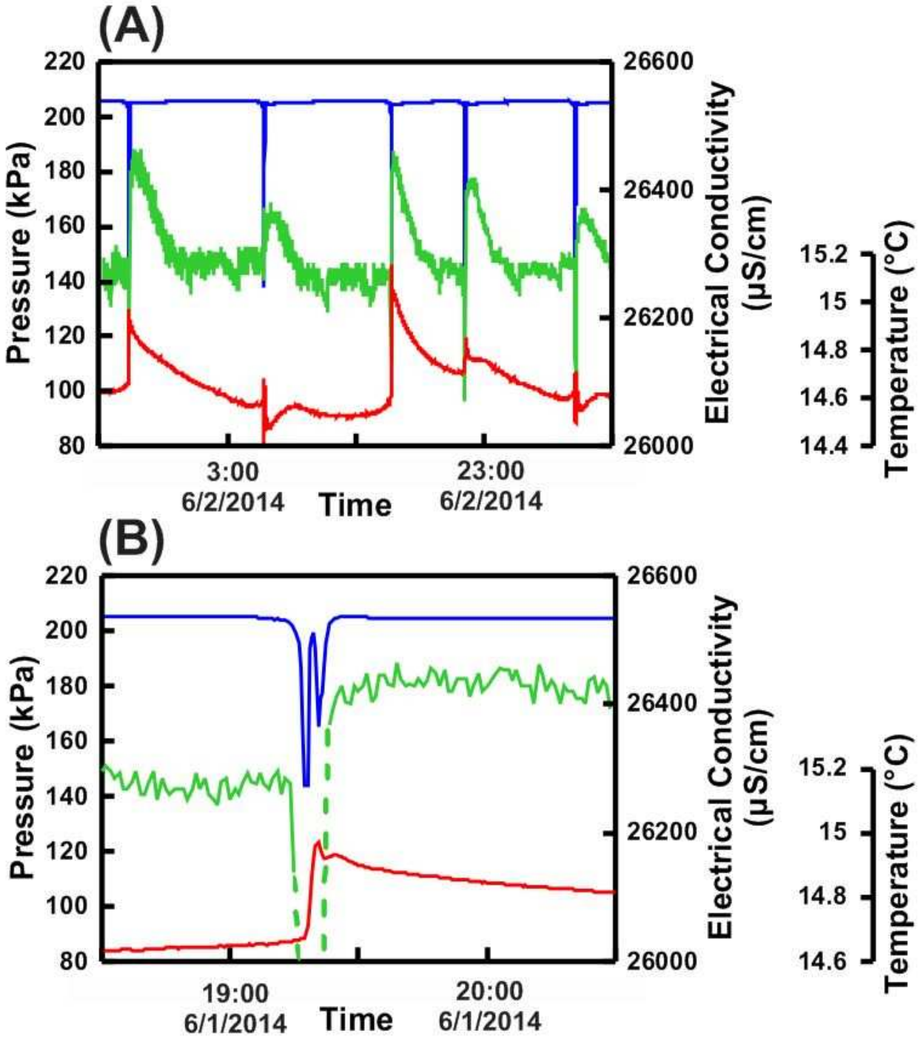

Figure 19. (A) Variations in the electrical conductivity (green), pressure (blue) and temperature (red) during eruptions at Tenmile geyser in 2014.

9.5 Interpretations of Chemical Variations

The changes presented in the previous section are significant in that no other geyser has ever been shown to go through such periodic and systematic changes in effluent chemistry. The repeating changes in effluent chemistry suggest that there is a change in the contribution of fluid from different sources coinciding with the eruptive styles seen at the surface. Specifically, during the MEP, the temperature and electrical conductivity decrease in conjunction with the variations of certain elements. All of these changes lend credence to a hypothesis that the Entrada formation increases its contribution of fluid during the MEP. Previous hypotheses on the source of water from Crystal geyser have focused primarily on the Navajo Sandstone and some component of brine. Thus these changes in chemistry highlight the significant lack of understanding surrounding the system which drives this geyser.

10. Inverse modeling

Inverse modeling is a method which attempts to derive a solution through the mixing of endmembers and through fluid-mineral reactions to determine the fractional contribution from each source. PHREEQC attempts to reconstruct all possible combinations of mixing, dissolution and precipitation which could lead to the desired final solution. Inputs to the models presented here were the measured pH, temperature, Na^+, Mg^{2+}, Ca^{2+}, K^+, HCO_3^-, Cl^- and SO_4^{2-}, $\delta^{18}O$ and δD. Fe^{2+} and Sr^{2+} were also included in the model due to the large differences in concentration between the Entrada and Navajo Sandstone (Fig. 11C). The exact input data is shown in Table 5. Measured pH within the aquifers ranged from 5.1 to 5.4. However the pH measured at the surface from these aquifers, which ranged from 6.1 to 6.5, was chosen to help the model develop more potential mixes. Endmembers included water from the Entrada Sandstone, Navajo Sandstone and fault brine. Fluid analyses of the aquifers adjacent to Crystal geyser collected by Kampman et al. (2014) were used to characterize the Entrada and Navajo Sandstones (Fig. 13).

Table 5. Input data for Inverse Modeling. All values are in mmol/L.

	mEP	**MEP**	**Entrada 98 m**	**Navajo 206 m**	**Navajo 224 m**	**Navajo 276 m**	**Navajo 322 m**	**Fault Brine**
Na^+	164.74	126.93	47.6	52.6	72.4	92.6	112.5	3990
Ca^{2+}	23.6	22.7	27.6	25.3	23.4	23.4	24.1	34.7
Mg^{2+}	8.2	7.6	10.7	10.5	10.1	10	10.1	60.91
K^+	8.4	7.0	3.3	5.2	6.0	6.6	7.2	107.4
Fe^{2+}	0.192	0.208	0.349	0.027	.024	0.015	0.037	0.006
Sr^{2+}	0.157	0.163	0.186	0.119	0.124	0.129	0.135	0.298
HCO_3^-	78.60	74.40	45.0	50.62	59.24	62.14	63.7	5.1
Cl^-	113.54	98.73	26.8	33.6	50.0	69.4	84.9	4231
SO_4^-	23.63	22.8	17.9	16.6	18.6	19.6	20.7	61.84
$\delta^{18}O$	-14.9	-15.0	-13.09	-15.63	-15.21	-14.84	-14.7	2.2
δD	-114.3	-115.38	-110.1	-116.7	-117.5	115.8	-114.6	-42.0

A representative profile of the chemical speciation of the Navajo Sandstone was developed from this dataset revealing large changes over depth. Due to these variations, which are predominately a function of depth, simulations were conducted using samples over depth; 206 mbs, 224 mbs, 276 mbs and 322 mbs. Only one sample was collected from the Entrada Sandstone (98 mbs) and is treated as representative of the formation's chemical speciation. To account for the elevated concentrations of Na^+, K^+, Cl^- and SO_4^{2-} at Crystal geyser compared to the Navajo and Entrada, Paradox Brine samples from Kharaka et al. (1997) were used as the third endmember. The $\delta^{18}O$ and δD values used in the brine are, however, from the Ismay Brine in the Paradox Zone (Spangler, 1992). Thus this conceptual model assumes that the fault brine directly reaches the well. Two output solutions were chosen, one for the mEP and the MEP. The values used as representing the mEP and MEP are from the 2014 data. In total 8 mixing models were developed to determine the fluid contribution for the mEP (4 models) and the MEP (4 models).

In order to develop mixing models based on the large number of input parameters, larger uncertainties are required. The uncertainties in PHREEQC allow for the alteration of each input in each solution prior to mixing. For example, if a sample has a K^+ concentration of 7.0 mmol/L and the uncertainty is 10%, the model can increase or decrease this concentration by 0.7 mmol/L prior to mixing. Thus the resulting mixing model is based on the mixing of altered input solutions. Ideally the alteration of the solutions will be small enough to where the model will still provide useful results. The uncertainty within the mixing models is 10% for the three endmembers and 15% for the Crystal geyser effluent. The 10% uncertainty can be considered quite reasonable for the Entrada Sandstone because large changes in chemistry can occur over depth, as seen in the Navajo, and only one sample exists for the entire 120 m thickness of the Entrada. Additionally, because the exact chemical speciation of the brine is not known the 10% uncertainty is warranted. The averaged mEP and MEP samples shown in Table 5 are from the data collected in 2014. The change in Na^+, K^+, Cl^-, Fe^{2+}, Sr^{2+} from the mEP to the MEP was 22%, 20%, 15%, 8% and 4%, respectively. Ideally the change occurring during mixing should be less than the observed change at the geyser and mEP and MEP fluid concentrations should not overlap. For example, if the MEP model increased the Cl- concentration and the mEP model decreased the Cl- concentration to the point where the values are nearly equal, the model would fail to represent what this study is interested in. Typically the concentrations of Na+ and Cl- would decrease prior to mixing for both mEP and MEP models, thereby maintaining the chemical differences in the respective fluids. In addition to fluid mixing, mineral or gas dissolution and precipitation can occur to account for the changes in ionic speciation. No precipitation or dissolution of minerals is allowed in this model because fluid mixing within the well will be rapid and it is not assumed that the minerals will be dissolving or precipitating as they migrate upwards. The only reaction occurring during the mixing was the degassing of CO_2 from solution. This is certainly a reasonable reaction given that CO_2 is constantly leaving solution at Crystal geyser.

Table 6. Inverse Modeling Results. N206mEP stands for the data used from 206 m depth in the Navajo Sandstone.

Minor Eruption	Navajo	Entrada	Brine
N206mEP	X	X	X
N224mEP	66.02%	32.77%	1.19%
N276mEP	X	X	X
N322mEP	66.34%	32.85%	0.79%

Major Eruption	Navajo	Entrada	Brine
N206MEP	53.71%	44.86%	1.41%
N224MEP	54.66%	43.96%	1.36%
N276MEP	53.63%	45.22%	1.12%
N322MEP	57.20%	41.90%	0.87%

11. Results

Rather consistent results were developed for each group of models for the mEP and MEP. Due to the large number of inputs and solutions, produced mixing models were few. Typically each model would produce one mixing scenario where the only reaction occurring was the degassing of CO_2. The percent contribution from the Navajo, Entrada and Brine for the mEP and MEP are shown in Table 6. In general, the Navajo decreases from a contribution of 66% to 53% from the mEP to the MEP. Conversely, the Entrada increases from 32% to 45% during the transition from the mEP to the MEP.

12. Inverse Modeling Results Discussion

Contrary to conventional hypotheses, the Entrada Sandstone supplies a significant fraction of the water (32-45%). All models imply that the fault brine consistently delivers water directly to the well and comprises 0.5-1.5% of the emanating fluid. Given that the well is open to the entire Entrada and Navajo Sandstone it should be inferred that water is sourced from all depths. The chemical speciation within the aquifers supplying Crystal geyser and the varying trends seen throughout the eruptions imply that the fractional contributions of brine and water from the Entrada and Navajo sandstone change throughout time. Specifically the contribution of fluid from the Navajo is greater during the mEP and the contribution from the Entrada increases during the MEP. Whether the change in effluent chemistry is a trigger or response to the eruptions is still not understood. Watson et al. (2014) proposed that the MEP at Crystal geyser must be driven by a gas accumulation due to the extensive lengths of the period. This hypothesis in conjunction with the observed trends in water characteristics and the results of inverse modeling suggest that the gas chamber driving the MEP occurs within the Entrada formation. Unfortunately, due to the rock clog within the well of Crystal geyser, no investigation of a gas chamber can be conducted.

The thicknesses of the Entrada and Navajo Sandstone aquifers are almost equal in the location of Crystal geyser. Thus the net volumetric contribution of the fluids should be dependent upon the hydraulic conductivity and the pressure gradient within the formations. Flow rates into the well with respect to a single formation should be greatest near the base due to overpressures increasing with depth (Kampman et al., 2014). However, as seen through the chemical variations, the discharge of fluid into well is heterogeneous with respect to a single formation and both formations. This heterogeneous flow creates a complex local pressure regime which is one of the predominant controls on the geysering seen at the surface. Based on the varying chemical characteristics of the emanating fluid from Crystal geyser, interpretations can be made about the physical interactions at depth. The Navajo Sandstone aquifer has a hydraulic conductivity five times greater than the Entrada Sandstone (528 vs. 100 md) (Hood and Patterson, 1984). As shown by the inverse modeling results, the Navajo Sandstone supplies the majority of the water during the mEP. The greater hydraulic conductivity of the Navajo Sandstone provides more water-dominated and mild eruptions. Thus, the smaller hydraulic conductivity for the Entrada constricts the available water supply and produces more vigorous eruptions during the MEP. Thus the contribution of from each aquifer based on the chemical speciation of the emanating fluid is coherent with the physical characteristics of the aquifers and the eruption styles. As proposed by the conceptual model in section 6.1, it is assumed that a large gas chamber drives the MEP. Based on the chemical variations, temperature decrease and results of inverse modeling, it should be assumed that this gas chamber occurs somewhere within the Entrada Sandstone. Unfortunately, due to the rock clog, investigating an open gas chamber connected to the well is impossible.

13. Discussion and Conclusion

13.1 Geyser Eruption Mechanism

Based on the observation of three cold-water geysers, a further insight is obtained after the studies of Lu et al. (2006) and Han et al. (2013). A conceptual model is presented in Fig. 20 to illustrate the eruption mechanism that initiates by an in-well CO_2-degassing feedback process. Initially, the artesian condition ($P_{formation} > P_{hydrostatic}$) causes CO_2-rich fluids to continually migrate upwards from the bottom (T1 in Fig. 20). Such reasoning can be supported by field observations of continuously increasing water level in between eruptions. Additionally, Kampman et al. (2014) observed that the primary aquifers supplying Crystal and Tenmile geysers (e.g., Entrada and Navajo Sandstones) have formation overpressures ranging from 0–1.3 MPa, while Keating et al. (2013) observed that the aquifers supplying Chimayó geyser are also heterogeneously over-pressured. The simulations conducted by Lu et al. (2006), Pruess (2008) and Pan et al. (2011) for CO_2-H_2O leakage through a wellbore also revealed that eruptions are initiated by large pressure differences between the formation and well. Formation permeability will be one of the primary factors governing the supply rate of CO_2-rich water and subsequently the interval between two separate eruptions. Simulations by Ingebritsen and

Rojstaczer (1993) for geothermal geysers indicated that increasing formation permeability would reduce the duration of an interval as the recharging process to the conduit is faster. In contrast, Chimayó geyser has long eruption intervals (20.4±5.6 hours) (Fig. 4B) because its wellbore is fully cased and thus slows down the recharge process. The predicted flow rate of water into the well is denoted by the length of arrows in Fig. 20.

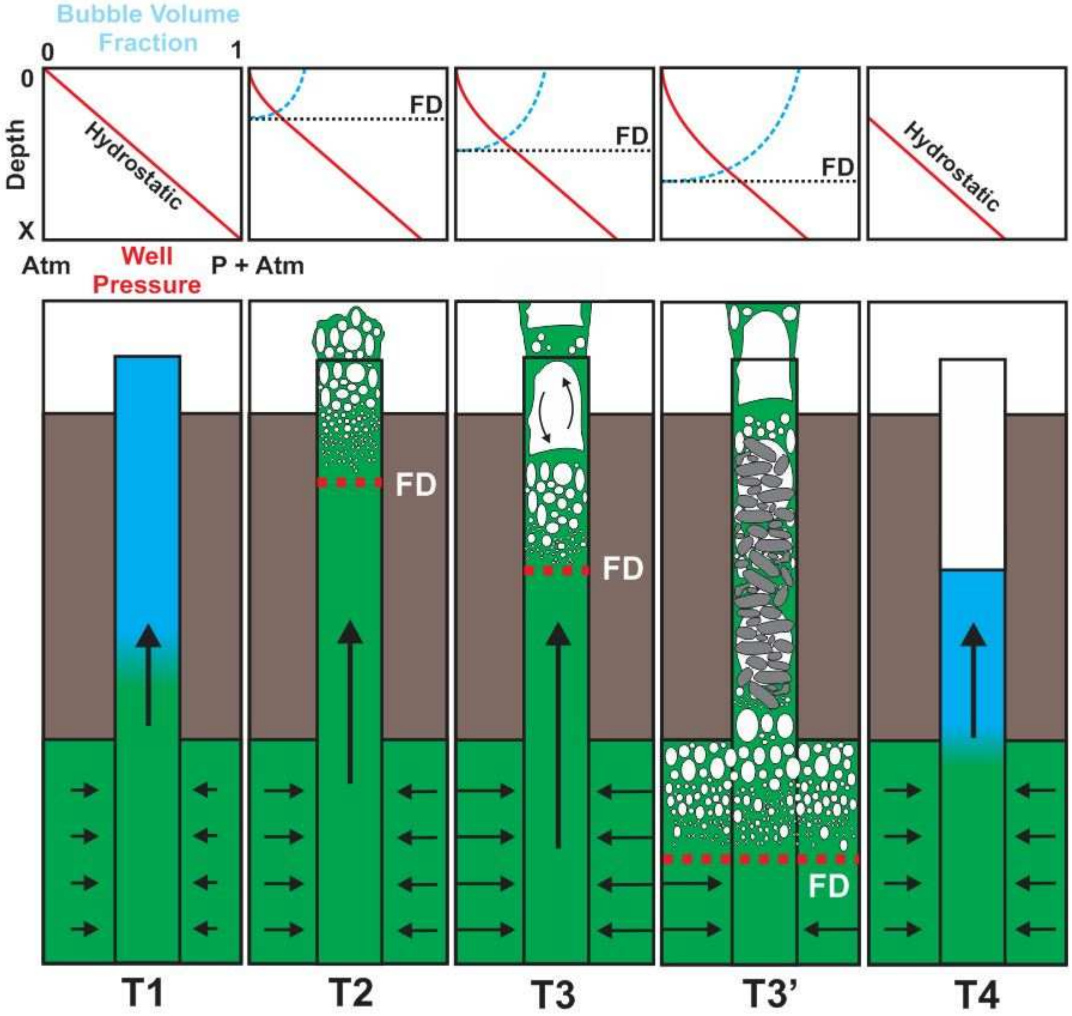

Figure 20. Conceptual model of the eruptive process. Green and blue colors are representative of CO_2 saturated and undersaturated waters, respectively. $CO_{2(g)}$ bubbles are shown in white and the flash depth (FD) is marked by the red dashed line. Plots showing the pressure (red line), flash depth (horizontal black dashed line) and bubble volume fraction (blue dashed line) over depth during the respective periods below.

As shown in T1 of Fig. 20, prior to eruptions all of the geysers reach the overflow point of the well head. No eruptions or degassing will occur until CO_2 becomes supersaturated in the water. Pressure reduction due to the upward migration of CO_2-rich fluids will initiate exsolution. The flash depth (FD) marks the point where $CO_{2(aq)}$ initially begins to exsolve. Above the FD, the exsolved CO_2 bubbles migrate upwards due to buoyancy forces that depend on the density difference of liquid water and $CO_{2(g)}$. Then the upwardly migrating CO_2 bubbles will reach terminal velocity (10-20 cm/s) when the drag and viscous forces are equal to the buoyant forces (Bozzano and Dente, 2001) (T2 in Fig. 20). The geyser eruptions take place as CO_2 bubbles continue to form by reducing the hydrostatic pressure, and consequently the FD deepens (from the surface) within the well. CO_2 bubble amalgamation will cause a rapid change in the internal pressure and shape of bubbles which subsequently alters the inertia, velocity and mass transfer in the bubbles (Lu et al., 2006). Eventually gas slugs or Taylor bubbles will form due to coalescence and excess $CO_{2(aq)}$ (T3 in Fig. 20). Taylor bubbles are large cylindrical bubbles which occupy the entire cross section of the well with rounded heads and flat sterns (bullet-shaped) with respect to the direction of motion. Recirculation within slugs will enhance heat and mass transfer at the liquid-gas interface (Salman et al., 2006) (Arrows inside slug in T3). The slugs will effectively push parcels of water upwards, developing liquid “slugs” in between, and create vigorous eruptions as observed in the three geysers discussed in this study. The development of $CO_{2(g)}$ or liquid slugs in the well is what causes the pulsing or surging eruptions seen. Once the eruption height reaches the maximum, the bubble volume fraction and flash depth will also reach their respective maximum accordingly (T3 in Fig. 20). Due to excessive degassing, eruptions will cease once the $CO_{2(aq)}$ concentration has reached a critical minimum, waiting for completion of another recharge (T4 in Fig. 20). Such combined processes of a CO_2-driven eruption exhibit self-enhancing and self-limiting characteristics and result in the periodic eruption scenarios observed.

The MEP at Crystal geyser is a continuous eruption period (currently lasting ~27 hours) as shown in Fig. 2D. This type of eruption does not fit the proposed conceptual model addressed above because, if it is generated by an in-well degassing process, the supply of $CO_{2(aq)}$ takes a considerably longer time to deplete compared to the preceding minor eruptions. Postulating a scenario where the supply of CO_2-rich water is suddenly much greater and continuous is difficult. Additionally, the revelations by Belousov et al. (2013) and Vandemeulebrouck et al. (2013) in hot water geysers have shown that periodic discharge of gas accumulations can drive eruptions. The discrepancy between the eruptions of the mEP and MEP at Crystal geyser therefore suggests that the MEP must be driven by an accumulation of compressible $CO_{2(g)}$ from the sourcing aquifers where the FD horizontally extends into the aquifer (T3’ in Fig. 20). Periodic discharge of water and CO_2 during the mEP leads to a progressive decrease in the pressure of the supplying formations. Then, this decreasing pressure condition enables $CO_{2(g)}$ to form and accumulate within the aquifers. Fracture networks in damaged zones, which might cross the well of Crystal geyser, could provide highly permeable pockets for gas accumulation. Once the pressure of the $CO_{2(g)}$ accumulation has reached the critical threshold, it will begin to discharge into the well. Further evidence of a gas accumulation driving the MEP is provided by observations just prior to the MEP where the discharge of liquid water (unaccompanied by $CO_{2(g)}$) rapidly increases for a few minutes and then is followed by vigorous eruptions. Presumably, the discharging gas slugs from depth push a large column of water up and out of the well. Kampman et al. (2014) found that rapid changes in emanating fluid temperatures and chemistry coincide with the onset of the MEP, suggesting that accumulation of gas occurs somewhere within the Entrada Sandstone formation (0-150 meters below the surface), which is shallower than the Navajo formation considered as the source aquifer of mEP.

13.2 Numerical Simulation of CO_2-Driven Cold-Water Geysers

In this section a 1-D non-isothermal multiphase pipe flow model is formulated to simulate the CO_2-driven geyser eruptions. The simulations based on this model may provide, at least qualitatively, further details about geyser eruption scenarios and a better understanding of the proposed conceptual model presented in the previous section. As an example, the parameters for Chimayó Geyser are used (Table 7) since the fluid-flowing profile in the cased wellbore can typically be described by pipe flow. Exact replication of the eruption periodicity is beyond the scope of this model; more so it is utilized to demonstrate how the thermo-physical properties of CO_2-H_2O mixtures affect the development of the flashing depth, CO_2 bubble volume fraction and eruption velocity. Details and discussions about this numerical model are given in Appendix B. Input parameters are provided in Table 7. Fig. 21A presents the simulated relationships between the flash depth, CO_2 bubble volume fraction, and mixture velocity profiles with the inlet velocity at 100 m depth varying from 1 m/s to 2 m/s. The profiles can be considered as snapshots of the in-well dynamics during an eruption.

Table 7. Cold-water geyser numerical simulation input parameters

Model Parameter	Value
Length of Well, (L)	100 m
Radius of Well, (R_w)	0.05 m
Deviation angle of Well, (θ)	0°
Overall heat transfer coefficient (U_{to})	1.0 J/ms°C
Surface Temperature ($T\|_{x=L}$) and **Surface Pressure ($p\|_{x=L}$)**	11.85°C 0.101 MPa
Bottomhole Temperature ($T\|_{x=0}$) **and Bottomhole Pressure ($p\|_{x=0}$)**	15.85°C 1.101 MPa
H_2O and CO_2 Mole Fraction **($z^0_{H_2O}$ and $z^0_{CO_2}$)**	0.96, 0.04
Joule-Thomson Coefficient (H_2O, CO_2) **($\eta_{L(H_2O)}$ and $\eta_{G(CO_{2\partial})}$)**	-0.22, 11.2 °C/MPa
Heat Capacity (H_2O, CO_2) **($C_{pL(H_2O)}$ and $C_{pG(CO_2)}$)**	4.18, 0.84 J/g°C
Inlet Velocity ($v_m\|_{x=0}$)	1, 1.25, 1.5, 1.75, 2 m/s

The flash depth can be identified by the CO_2 bubble volume fraction when it deviates from 0. Phase transition occurs at this depth where the pure liquid state of the mixture turns to two-phase with the presence of $CO_{2(g)}$. This transition causes a sharp increase in the mixture velocity where the acceleration is greatest immediately above the flash depth. It can be seen from Fig. 21A that lower inlet velocities result in shallower flash depths and lead to smaller gaseous CO_2 volume fraction and smaller exit velocities at the surface. We may take the profile with 1 m/s inlet velocity to be a representative of T2 in Fig. 20. With this, the hydrostatic pressure decreases constantly as the CO_2 continues to degas above the flashing depth. Beyond T2, the decreasing flash depth and increasing CO_2 bubble volume fraction enhance the velocity of both the mixture and inlet. Fig. 21A also shows that when the flash depth reaches the deepest level, the exit velocity reaches the highest, as illustrated in T3 in Fig. 20. It is noted that while the inlet velocity here is treated to be an input parameter, in a natural CO_2-driven geyser it will be governed by the self-enhancing and limiting processes of an eruption such as bubble growth and pressure decrease.

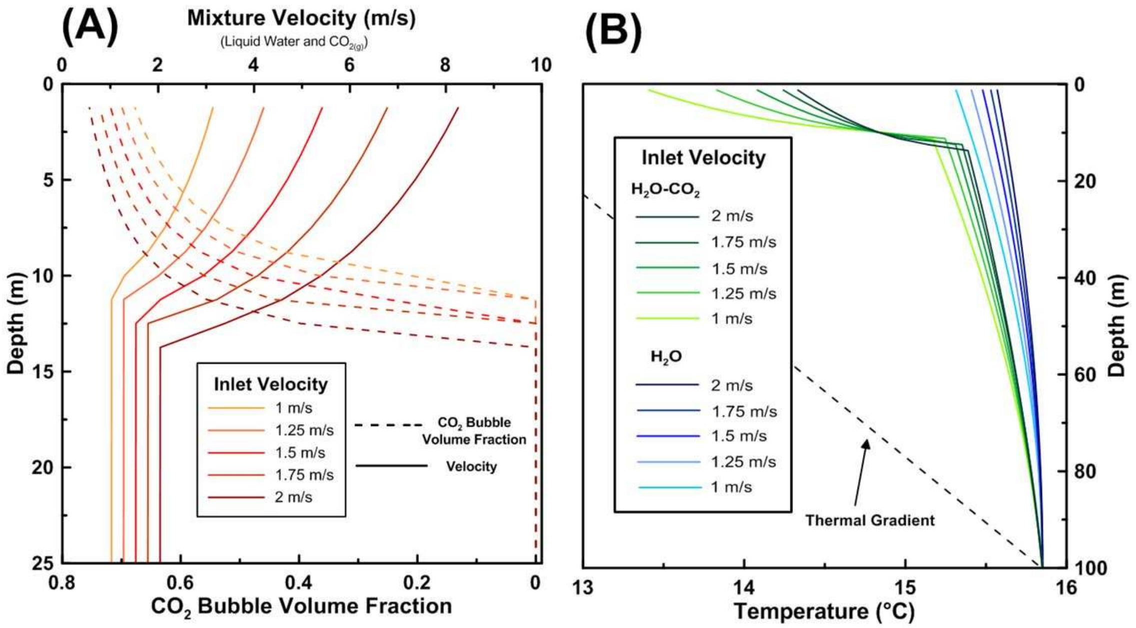

Figure 21. Simulation results of (A) mixture velocity (liquid water and $CO_{2(g)}$) (solid lines) and CO_2 bubble volume fraction (dashed lines) and (B) temperature over depth.

The temperature profiles of the mixture (CO_2-H_2O) were investigated to understand the degree of thermal alteration resulting from the CO_2 degassing and thermal conduction effect (Fig. 21B). As a reference, Fig. 21B also presents the temperature profiles of pure liquid water where no degassing effect is involved. For this pure liquid water, the effect of thermal conduction on the water is greatest with the slowest flow rate (1 m/s). It is shown that when the water, initially at 15.85 °C, migrates from 100 m depth to the surface, its temperature would drop around 0.5°C. This is because the fluid is warmer than its geological surroundings (at the bottom the fluid was set to be at a thermal equilibrium state with its surroundings); when it moves upwards along the wellbore, the slower the fluid flows, the more heat it loses. In contrast, for the fastest moving liquid water (e.g., 2 m/s) the temperature only drops about 0.3°C because it loses less heat to the surroundings. This trend is also retained for a mixture of H_2O and CO_2 before reaching the flashing depth, as shown in Fig. 21B. After the flash depth (10 to 15 m), rapid reduction of temperature occurs because generation and growth of CO_2 bubbles are accompanied by the endothermic effect of CO_2 exsolution and Joule-Thomson cooling. The range of temperature reduction was approximately 1-2°C in this example. Validation of the temperature changes simulated within a geysering wellbore by field measurements has yet to be conducted as it requires a multitude of measurement points during a single monitoring period. This warrants the merit of a further study as it could provide another relationship between the CO_2-driven eruptive behavior and its relevant thermal changes.

13.3 Geysering Wellbores in Carbon Capture and Storage Facilities

As proposed by the conceptual model in Fig. 20, a typical wellbore configuration would provide the conduit geometry required for eruptions. The hydrologic setting of the geysers studied here would be analogous to a Carbon Capture Storage (CCS) site where stored CO_2 has leaked into a shallow aquifer. At a CCS site, an intruding CO_2 plume could provide the over-pressures required to drive CO_2-rich fluids upwards or cause supersaturation of CO_2 at the formation depth (Pruess, 2008). The historical accounts and analysis of the wellbore geysers show that eruptions can be fueled for decades and possibly centuries but whether the periodicity and intensity will change over time is difficult to discern (Fig. 4). The MEP at Crystal geyser highlights the potential for a wellbore to develop into continuous leakage. Though we propose that to sustain such a long eruption period, the proper geometry or traps must exist at depth to allow for the accumulation of $CO_{2(g)}$. Additionally, because Crystal geyser is not cased, it has a surface area of 289.8 m^2 in contact with water bearing units (Entrada and Navajo Sandstone) which help sustain discharge for over 24 hours. Chimayó geyser most accurately represents the eruptions that would be seen at a CCS site primarily due to having a casing which will limit the supply of H_2O-CO_2 and duration of eruptions.

As evidenced by the large difference in emission of CO_2 from the presented geysers, the degree of leakage will be dependent upon the casing condition, length and diameter of wells, the CO_2-saturation of fluids, sourcing aquifer conditions (pressure and temperature) and, especially, the ratio of eruptive to quiet time. Thus understanding the hydrologic properties of rock units in which wells are screened could provide valuable data for determining the risk for eruptions to occur and be sustained for long periods of time. The emission of CO_2 from Tenmile and Chimayó geysers ($(6.17\pm1.73)\times10^1$ t/yr and $(6.54\pm0.57)\times10^1$ t/yr) are comparable to that of slowly forming travertine deposits (Burnside et al., 2013). As determined by Burnside et al. (2013), travertine mounds along the Little Grand Wash and Salt Wash fault systems had deposition rates ranging $(0.10\text{-}8.71)\times10^2$ t/yr and $(0.20\text{-}8.00)\times10^1$ t/yr of CO_2, respectively. The rate of deposition (8.71×10^2 t/yr) from largest travertine mound analyzed by Burnside et al. (2013), L4, exceeds that of Tenmile and Chimayó geyser but is over a much larger area. Thus, even small CO_2-driven geysers like Tenmile or Chimayó geyser that have small eruptive to quiet period ratios present, on a spatial scale, the sources of most rapid leakage. While the discharge of CO_2 from geysering wells has been shown to reach significant rates, the conditions which allow geysering to occur are fleeting and will not be sustained like travertine deposition or fault zone $CO_{2(g)}$ flux. Furthermore, CO_2-driven geysers are surficial expressions of leakage already occurring in the subsurface; a very difficult problem to mitigate. Thus, while wellbores which develop into CO_2-driven geysers have the potential to reach significant leakage rates, they still present a smaller risk due to being point specific and easily identifiable phenomena.

REFERENCES

Allis, R., Bergfeld, D., Moore, J., McClure, K., Morgan, C., Chidsey, T.C., Heath, J., McPherson, B.J., 2005. Implications of results from CO_2 flux surveys over known CO_2 systems for long-term monitoring, The 4th Annual Conference on Carbon Capture and Sequestration, Alexandria, VA.

Annamalai, K., Puri, I.K., 2002. Advanced Thermodynamics Engineering. CRC Press, Boca Raton.

Assayag, N., Bickle, M., Kampman, N., J., B., 2009. Carbon isotopic constraints on CO_2 degassing in cold-water Geysers, Green River, Utah. Energy Procedia 1, 6.

Baer, J.L., Rigby, J.K., 1978. Geology of the Crystal Geyser and environmental implications of its effluent, Grand County, Utah, Utah Geology, pp. 125-130.

Barton, J.R., Fuhriman, D.K., 1973. Crystal Geyser Project: A Study of Some Alternative Methods for Eliminating the Salt Contribution of Crystal Geyser from the Green River. Center for Environmental Studies, Brigham Young University, 55.

Batzle, M., Wang, Z., 1992. Seismic Properties of Pore Fluids. Geophysics 57, 1396-1408.

Belousov, A., Belousova, M., Nechayev, A., 2013. Video observations inside conduits of erupting geysers in Kamchatka, Russia, and their geological framework: Implications for the geyser mechanism. Geology 41, 387-390.

Bickle, M., Kampman, N., 2013. Lessons in carbon storage from geological analogues. Geology 41, 525-526.

Bozzano, G., Dente, M., 2001. Shape and terminal velocity of single bubble motion: a novel approach. Comput. Chem. Eng. 25, 571-576.

Burnside, N.M., Shipton, Z.K., Dockrill, B., Ellam, R.M., 2013. Man-made versus natural CO_2 leakage: A 400 k.y. history of an analogue for engineered geological storage of CO_2. Geology 41, 471-474.

Celia, M.A., Bachu, S., Nordbotten, J.M., Gasda, S.E., Dahle, H.K., 2004. Quantitative estimation of CO_2 leakage from geological storage: analytical models, numerical models, and data needs, in: Rubin, E.S., Keith, D.W., Gilboy, C.F., Wilson, M., Morris, T., Gale, J., Thaambimuthu, K. (Eds.), 7th International Conference on Greenhouse Gas Control Technologies 5. Elsevier, Vancouver, Canada, pp. 663-671.

Doelling, H., 1994. Tufa Deposits in Western Grand County. Utah Geological Survey, "Survey Notes", 26, 28-13.

Duan, Z., Hu, J., Li, D., Mao, S., 2008. Densities of CO_2-H_2O and CO_2-H_2O-NaCl Systems Up to 647 K and 100 MPa. Energ. Fuel. 22, 1666-1674.

Duan, Z., Sun, R., 2003. An improved model calculating CO_2 solubility in pure water and aqueous NaCl solutions from 273 to 533 K and from 0 to 2000 bar. Chem. Geol. 193, 257-271.

Friedmann, S.J., 2007. Geological Carbon Dioxide Sequestration. Elements 3, 179-184.

Glennon, J.A., Pfaff, R.M., 2005. The operation and geography of carbon dioxide-driven, cold-water “geysers”. The GOSA Trans. 9, 184-192.

Gouveia, F.J., Friedmann, S.J., 2006. Timing and prediction of CO_2 eruptions from Crystal Geyser, UT. Lawrence Livermore National Laboratory Technical Report, UCRL-TR-221731, pp. 1-14.

Gouveia, F.J., Johnson, M.R., Leif, R.N., Friedmann, S.J., 2005. Aerometric measurement and modeling of the mass of CO_2 emissions from Crystal Geyser, Utah.

Lawrence Livermore National Laboratory Technical Report, UCRL-TR-211870, pp. 1-57.

Han, W.S., Lu, M., McPherson, B.J., Keating, E.H., Moore, J., Park, E., Watson, Z.T., Jung, N.-H., 2013. Characteristics of CO_2-driven cold-water geyser, Crystal Geyser in Utah: experimental observation and mechanism analyses. Geofluids 13, 283-297.

Hasan, A.R., Kabir, C.S., 2002. Fluid flow and heat transfer in wellbores. Soc. Petrol. Eng. J., 181.

Heath, J.E., Lachmar, T.E., Evans, J.P., Kolesar, P.T., Williams, A.P., 2009. Hydrogeochemical Characterization of Leaking, Carbon Dioxide-Charged Fault Zones in East-Central Utah, With Implications for Geologic Carbon Storage, in: McPherson, B.J., Sundquist, E.T. (Eds.), Carbon Sequestration and Its Role in the Global Carbon Cycle. American Geophysical Union, Washington, D.C., pp. 147-158.

Hood, J.W., Patterson, D.J., 1984. Bedrock Aquifers in the Northern San Rafael Swell area, Utah, with special emphasis on the Navajo Sandstone, State of Utah Department of Natural Resources Technical Publication, 78, pp. 1-128.

Hu, L., Pan, L., Zhang, K., 2012. Modeling brine leakage to shallow aquifer through an open wellbore using T2WELL/ECO2N. International Journal of Greenhouse Gas Control 9, 393-401.

Hurwitz, S., Hunt, A.G., Evans, W.C., 2012. Temporal variations of geyser water chemistry in the Upper Geyser Basin, Yellowstone National Park, USA. Geochem. Geophy. Geosy. 13, 1-19.

Hurwitz, S., Sohn, R.A., Luttrell, K., Manga, M., 2014. Triggering and modulation of geyser eruptions in Yellowstone National Park by earthquakes, earth tides, and weather. J. Geophy. Res.-Solid 119, 1718-1737.

Hutchinson, R.A., Westphal, J.A., Kieffer, S.W., 1997. In situ observations of Old Faithful Geyser. Geology 25, 875-878.

Ingebritsen, S.E., Rojstaczer, S.A., 1993. Controls on Geyser Periodicity. Science 262, 889-892.

IPCC, 2005. IPCC Special Report on Carbon Dioxide Capture and Storage, in: Metz, B., Davidson, O., Coninck, H.C.d., Loos, M., Meyer, L.A. (Eds.), Cambridge University, p. 442.

Jordan, P.D., Benson, S.M., 2009. Well blowout rates and consequences in California Oil and Gas District 4 from 1991 to 2005: implications for geological storage of carbon dioxide. Environ. Geol. 57, 1103-1123.

Jung, N.-H., Han, W.S., Watson, Z.T., Graham, J.P., Kim, K.-Y., 2014. Fault-controlled CO_2 leakage from natural reservoirs in the Colorado Plateau, East-Central Utah. Earth Planet. Sc. Lett. 403, 358-367.

Kampman, N., Bickle, M., Becker, J., Assayag, N., Chapman, H., 2009. Feldspar dissolution kinetics and Gibbs free energy dependence in a CO_2-enriched groundwater system, Green River, Utah. Earth Planet. Sc. Lett. 284, 473-488.

Kampman, N., Bickle, M.J., Maskell, A., Chapman, H.J., Evans, J.P., Purser, G., Zhou, Z., Schaller, M.F., Gattacceca, J.C., Bertier, P., Chen, F., Turchyn, A.V., Assayag, N., Rochelle, C., Ballentine, C.J., Busch, A., 2014. Drilling and sampling a natural CO_2

reservoir: Implications for fluid flow and CO_2-fluid-rock reactions during CO_2 migration through the overburden. Chem. Geol. 369, 51-82.

Kampman, N., Burnside, N.M., Shipton, Z.K., Chapman, H.J., Nicholl, J.A., Ellam, R.M., Bickle, M.J., 2012. Pulses of carbon dioxide emissions from intracrustal faults following climatic warming. Nat. Geosci. 5, 352-358.

Karlstrom, L., Hurwitz, S., Sohn, R., Vandemeulebrouck, J., Murphy, F., Rudolph, M.L., Johnston, M.J.S., Manga, M., McCleskey, R.B., 2013. Eruptions at Lone Star Geyser, Yellowstone National Park, USA: 1. Energetics and eruption dynamics. J. Geophys. Res.-Solid 118, 4048 - 4062.

Keating, E.H., Fessenden, J., Kanjorski, N., Koning, D.J., Pawar, R., 2010. The impact of CO_2 on shallow groundwater chemistry: observations at a natural analog site and implications for carbon sequestration. Env. Earth Sci. 60, 521-536.

Keating, E.H., Hakala, J.A., Viswanathan, H., Carey, J.W., Pawar, R., Guthrie, G.D., Fessenden-Rahn, J., 2013. CO_2 leakage impacts on shallow groundwater: Field-scale reactive-transport simulations informed by observations at a natural analog site. Appl. Geochem. 30, 136 - 147.

Kharaka, Y.K., Ambats, G., Thordsen, J.J., 1997. Deep well injection of brine from Paradox Valley, Colorado: Potential major precipitation problems remediated by nanofiltration. Water Resources Research 33, 1013-1020.

Kieffer, S.W., 1989. Geologic Nozzles. Rev. Geophys. 27, 3-38.

Lewicki, J.L., Evans, W.C., Hilley, G.E., Sorey, M.L., Rogie, J.D., Brantley, S.L., 2003. Shallow soil CO_2 flow along the San Andreas and Calaveras Faults, California. J. Geophys. Res.-Solid 108, 2187-2200.

Lu, M., Connell, L.D., 2014. Transient, thermal wellbore flow of multispecies carbon dioxide mixture with phase transition during geological storage. Int. J. Multiphase Flow 63, 82-92.

Lu, X., Watson, A., Gorin, A.V., Deans, J., 2005. Measurements in a low temperature CO_2-driven geysering well, viewed in relation to natural geysers. Geothermics 34, 389-410.

Lu, X., Watson, A., Gorin, A.V., Deans, J., 2006. Experimental investigation and numerical modelling of transient two-phase flow in a geysering geothermal well. Geothermics 35, 409-427.

Malekzadeh, R., Belfroid, S.P.C., Mudde, R.F., 2012. Transient drift flux modelling of severe slugging in pipeline-riser systems. Int. J. Multiphase Flow 46, 32-37.

Mastin, L.G., 1995. Thermodynamics of gas and steam-blast eruptions. B. Volcanol. 57, 85-98.

Mayo, A.L., Shrum, D.B., Jr., T.C.C., 1991. Factors contributing to exsolving carbon dioxide in the ground water systems in the Colorado Plateau, Utah. Utah Geological Association, 335-341.

Nicholl, M.J., Wheatcraft, S.W., Tyler, S.W., Berkowitz, B., 1994. Is Old Faithful a strange attractor? J. Geophys. Res.-Solid 99, 4495-4503.

Noguchi, K., Nix, J., 1963. Geochemical studies of some geysers in Yellowstone National Park. Proceedings of the Japan Academy 39, 370-375.

Oldenburg, C.M., 2011. Health, safety, and environmental risks from energy production: a year-long reality check. Greenhouse Gases: Sci. and Tech. 1, 102-104.

Pan, L., Oldenburg, C.M., Pruess, K., Wu, Y.-S., 2011. Transient CO_2 leakage and injection in wellbore-reservoir systems for geologic carbon sequestration. Greenhouse Gases: Sci. and Tech. 1, 335-350.

Peng, D.-Y., Robinson, D.B., 1976. A new two-constant equation of state. Ind. Eng. Chem. Fund. 15, 59-64.

Pruess, K., 2008. On CO_2 fluid flow and heat transfer behavior in the subsurface, following leakage from a geologic storage reservoir. Environ. Geol. 54, 1677-1686.

Rinehart, J.S., 1980. Geysers and Geothermal Energy. Springer-Verlag, New York.

Ross, K., 1997. Cold Water Geysers in Southern Utah. The GOSA Sput 11, 14-15.

Salman, W., Gavriilidis, A., Angeli, P., 2006. On the formation of Taylor bubbles in small tubes. Chem. Eng. Sci. 61, 6653 - 6666.

Shi, H., Holmes, J., Durlofsky, L., Aziz, K., Diaz, L., Alkaya, B., Oddie, G., 2005. Drift flux modelling of two-phase flow in wellbores. Soc. Petrol. Eng. J. 10, 24-33.

Shipton, Z.K., Evans, J.P., Dockrill, B., Heath, J., Williams, A., Kirchner, D., Kolesar, P.T., 2005. Natural Leaking CO_2-Charged Systems as Analogs for FailedGeologic Storage Reservoirs, in: Thomas, D.C. (Ed.), Carbon Dioxide Capture for Storage in Deep Geologic Formations - Results from the CO_2 Capture Project. Elsevier, pp. 699-712.

Shipton, Z.K., Evans, J.P., Kirschner, D., Kolesar, P.T., Williams, A.P., Heath, J.E., 2004. Analysis of CO_2 leakage through "low-permeability" faults from natural reservoirs in the Colorado Plateau, east-central Utah. Geological Society of London Special Publications 233, 43-58.

Span, R., Wagner, W., 1996. A new equation of state for carbon dioxide covering the fluid region from the triple-point temperature to 1100 K at pressures up to 800 MPa. J. Phys. Chem. Ref. Data 25, 1509-1596.

Spangler, L.E., 1992. Records of wells in sandstone and alluvial aquifers and chemical data for water from selected wells in the Navajo aquifer in the vicinity of the greater Aneth oil field, San Juan County, Utah. U.S. Geological Survey, pp. 1-44.

Vandemeulebrouck, J., Roux, P., Cros, E., 2013. The plumbing of Old Faithful Geyser revealed by hydrothermal tremore. Geophy. Res. Lett. 40.

Watson, Z.T., Han, W.S., Keating, E., Jung, N.-H., Lu, M., 2014. Eruption dynamics of CO2-driven cold-water geysers: Crystal, Tenmile geysers in Utah and Chimayo geyser in New Mexico. Earth and Planetary Science Letters 408, 272-284.

Willhite, G.P., 1967. Over-all heat transfer coefficients in steam and hot water injection wells. J. Petrol. Technol. 19, 607-615.

Zhang, Y., 1996. Dynamics of CO_2-driven lake eruptions. Nature 379, 57-59.

Zuber, N., Findlay, J.A., 1965. Average volumetric concentration in two-phase flow systems. J. Heat Transfer 87, 453-468.

APPENDIX A

1. Kampman et al. 2014, November 2007

ID	**Time**	**pH**	**Major Cations (mmol/L)**				**Major Anions (mmol/L)**			**Minor**	
			Na^+	**K^+**	**Ca^{2+}**	**Mg^{2+}**	**SO_4^{2-}**	**Cl^-**	**HCO_3^-**	**Sr^{2+}**	**Fe^{2+}**
CG1	12:00	6.32	163.56	9.35	26.13	9.63	25.58	122.7	ND	0.15	ND
CG2	12:30	6.38	164.41	9.37	26.27	9.64	25.47	124.1	ND	0.15	ND
CG3	13:00	6.38	166.21	9.46	26.11	9.61	25.57	125.7	ND	0.15	ND
CG4	13:30	6.38	169.29	9.64	26.31	9.73	26.03	129.2	ND	0.15	ND
CG5	14:00	6.38	169.69	9.66	25.84	9.67	25.97	127.8	ND	0.15	ND
CG6	14:30	6.37	168.38	9.58	26.03	9.54	25.78	122.2	ND	0.15	ND
CG7	15:00	6.31	168.87	9.52	25.94	9.52	25.87	122.6	ND	0.15	ND
CG8	15:30	6.38	170.81	9.67	25.71	9.61	26.10	129.6	ND	0.15	ND
CG9	15:47	6.57	170.65	9.61	26.33	9.56	26.07	129.3	ND	0.15	ND
CG10	15:55	6.57	162.50	9.36	26.45	9.71	25.47	123.4	ND	0.15	ND
CG11	16:02	6.55	160.07	9.22	26.32	9.64	25.03	120.8	ND	0.15	ND
CG12	16:06	6.57	158.24	9.12	26.24	9.64	25.01	121.6	ND	0.15	ND
CG13	16:10	6.55	158.09	9.14	26.50	9.70	24.91	118.8	ND	0.15	ND
CG14	16:16	6.55	156.75	9.07	26.48	9.76	25.21	116.5	ND	0.15	ND
CG15	16:33	6.55	148.57	8.58	26.73	9.97	24.46	112.3	ND	0.15	ND
CG16	17:00	6.53	133.06	8.09	26.81	10.21	23.33	96.6	ND	0.16	ND
CG17	17:30	6.56	127.74	7.82	26.67	10.22	22.94	97.9	ND	0.16	ND

2. Kampman et al. 2014, September 2010 (2010a)

ID	**Time**	**pH**	**Major Cations (mmol/L)**				**Major Anions (mmol/L)**			**Minor**	
			Na^+	**K^+**	**Ca^{2+}**	**Mg^{2+}**	**SO_4^{2-}**	**Cl^-**	**HCO_3^-**	**Sr^{2+}**	**Fe^{2+}**
TS001a	15:55	ND	170.89	5.65	23.87	9.00	23.35	141.51	ND	ND	ND
TS001b	16:40	ND	172.22	5.71	24.66	9.10	23.79	139.86	ND	ND	ND
TS002	16:55	ND	160.54	5.51	25.20	9.35	23.20	126.44	ND	ND	ND
TS003	17:10	ND	160.13	5.50	23.91	9.39	23.18	126.38	ND	ND	ND
TS004	17:25	ND	157.69	5.45	25.43	9.32	22.96	126.76	ND	ND	ND
TS005	17:40	ND	161.28	5.59	21.59	9.66	23.25	125.70	ND	ND	ND
TS006	17:55	ND	156.52	5.40	24.86	9.35	22.80	124.24	ND	ND	ND
TS007	18:10	ND	155.03	5.43	25.26	9.34	22.75	123.30	ND	ND	ND
TS008	18:25	ND	155.06	5.42	25.37	9.44	22.96	122.40	ND	ND	ND
TS009	18:40	ND	151.51	5.36	24.38	9.37	22.40	120.79	ND	ND	ND
TS010	18:55	ND	151.60	5.36	25.12	9.39	22.53	119.27	ND	ND	ND
TS011	19:10	ND	150.53	5.33	24.00	9.42	22.38	117.90	ND	ND	ND
TS012	19:25	ND	145.71	5.20	25.22	9.39	22.03	116.03	ND	ND	ND
TS013	19:40	ND	141.47	5.10	24.58	9.38	21.64	115.28	ND	ND	ND
TS015	19:55	ND	138.64	5.05	24.57	9.53	21.59	107.93	ND	ND	ND
TS016	20:10	ND	135.80	4.98	25.13	9.50	21.33	108.82	ND	ND	ND
TS017	20:25	ND	134.46	4.94	25.30	9.59	21.44	106.12	ND	ND	ND

3. This Study, December 2010 (2010b1 and b2). B1 is 12/13/2010 and B2 is 12/15/2010

Date	**Time**	**pH**	**Major Cations (mmol/L)**				**Major Anions (mmol/L)**			**Minor (mmol/L)**	
			Na^+	**K^+**	**Ca^{2+}**	**Mg^{2+}**	**SO_4^{2-}**	**Cl^-**	**HCO_3^-**	**Sr^{2+}**	**Fe^{2+}**
12/13	8:57	6.53	169.05	8.12	22.54	8.88	18.80	106.33	61	0.15	0.19
12/13	9:27	6.55	175.34	8.39	23.32	9.28	19.79	113.42	95	0.16	0.19
12/13	9:54	6.55	180.56	8.59	25.43	9.23	19.86	114.84	63	0.15	0.19
12/13	10:21	6.53	129.90	6.18	21.58	7.02	20.23	115.29	77	0.13	0.14
12/13	10:45	6.56	165.82	7.87	21.88	8.51	19.89	114.93	67	0.14	0.17
12/13	12:45	6.59	185.69	8.87	26.34	9.76	19.99	113.85	77	0.16	0.21
12/13	12:52	6.51	174.97	8.69	26.67	10.04	19.33	107.23	75	0.16	0.21
12/13	13:02	6.51	174.71	8.74	26.87	10.08	19.18	107.69	57	0.16	0.21
12/13	13:12	6.52	175.73	8.77	26.99	10.08	19.28	106.19	77	0.16	0.21
12/13	13:22	6.53	174.12	8.70	26.60	10.16	19.37	106.74	76	0.16	0.20
12/13	13:32	6.52	176.95	8.89	27.08	10.19	19.43	107.33	92	0.16	0.20
12/15	10:18	6.57	153.82	7.51	21.40	9.94	19.95	113.53	83	0.16	0.20
12/15	10:48	6.54	179.90	9.00	27.38	10.40	16.76	60.60	35	0.16	0.20
12/15	11:18	6.56	173.55	8.87	27.22	10.23	19.57	106.72	77	0.16	0.21
12/15	11:48	6.58	164.13	8.69	27.56	10.58	18.56	98.77	77	0.17	0.22
12/15	12:18	6.55	139.41	7.34	26.46	10.70	17.92	92.91	75	0.17	0.21
12/15	12:48	6.57	150.19	8.34	27.93	10.77	17.45	90.69	60	0.17	0.21
12/15	13:18	6.57	133.69	7.33	26.15	10.88	17.42	89.51	57	0.17	0.21

12/15	13:48	6.56	147.03	8.32	28.38	10.90	17.22	87.97	54	0.17	0.22
12/15	14:18	6.46	137.16	7.80	27.07	11.01	17.83	89.21	73	0.17	0.22
12/15	14:33	6.58	132.56	7.36	27.30	11.18	16.94	87.02	55	0.18	0.22
12/15	14:48	6.6	143.99	8.20	28.11	11.07	17.21	87.85	62	0.17	0.22

4. This Study, May/June 2013

Date	**Time**	**pH**	**Major Cations (mmol/L)**				**Major Anions (mmol/L)**			**Minor (mmol/L)**	
			Na^+	**K^+**	**Ca^{2+}**	**Mg^{2+}**	**SO_4^{2-}**	**Cl^-**	**HCO_3^-**	**Sr^{2+}**	**Fe^{2+}**
5/30	13:50	ND	132.49	ND	ND	ND	ND	111.80	ND	ND	ND
5/30	14:02	ND	125.26	ND	ND	ND	ND	123.37	ND	ND	ND
5/30	14:13	ND	125.58	ND	ND	ND	ND	107.19	ND	ND	ND
5/30	14:26	ND	130.08	ND	ND	ND	ND	110.45	ND	ND	ND
5/30	14:44	ND	129.05	ND	ND	ND	ND	109.33	ND	ND	ND
5/30	14:56	ND	126.74	ND	ND	ND	ND	109.51	ND	ND	ND
5/30	15:30	ND	136.09	ND	ND	ND	ND	128.86	ND	ND	ND
5/30	16:02	ND	128.44	ND	ND	ND	ND	107.03	ND	ND	ND
5/30	16:30	ND	125.28	ND	ND	ND	ND	106.21	ND	ND	ND
5/30	17:30	ND	121.73	ND	ND	ND	ND	104.59	ND	ND	ND
5/30	18:00	ND	117.40	ND	ND	ND	ND	103.80	ND	ND	ND
5/30	18:30	ND	118.88	ND	ND	ND	ND	104.64	ND	ND	ND

5/30	19:07	ND	119.36	ND	ND	ND	ND	105.12	ND	ND	ND
5/30	19:45	ND	118.74	ND	ND	ND	ND	103.57	ND	ND	ND
5/30	20:36	ND	122.41	ND	ND	ND	ND	104.47	ND	ND	ND
5/30	21:10	ND	130.41	ND	ND	ND	ND	104.46	ND	ND	ND
5/30	21:40	ND	108.39	ND	ND	ND	ND	104.38	ND	ND	ND
5/30	22:15	ND	108.31	ND	ND	ND	ND	105.06	ND	ND	ND
5/30	22:45	ND	112.76	ND	ND	ND	ND	105.21	ND	ND	ND
5/31	9:20	ND	106.15	ND	ND	ND	ND	101.66	ND	ND	ND
5/31	10:00	ND	107.25	ND	ND	ND	ND	101.56	ND	ND	ND
5/31	10:41	ND	108.99	ND	ND	ND	ND	102.01	ND	ND	ND
5/31	11:35	ND	107.04	ND	ND	ND	ND	101.59	ND	ND	ND
6/3	14:40	ND	135.72	ND	ND	ND	ND	135.85	ND	ND	ND
6/3	14:53	ND	122.87	ND	ND	ND	ND	117.57	ND	ND	ND
6/3	15:07	ND	118.02	ND	ND	ND	ND	112.12	ND	ND	ND

5. This Study, May/June 2014

Date	**Time**	**pH**	**Major Cations (mmol/L)**				**Major Anions (mmol/L)**			**Minor (µmol/L)**	
			Na^+	**K^+**	**Ca^{2+}**	**Mg^{2+}**	**SO_4^{2-}**	**Cl^-**	**HCO_3^-**	**Sr^{2+}**	**Fe^{2+}**
5/30	12:35	6.37	127.75	7.0	22.79	7.6	21.74	89.03	60.0	163	207

5/30	14:46	6.35	124.29	6.9	21.97	7.4	21.75	88.54	69.0	164	208
5/30	16:45	6.43	126.38	7.0	22.76	7.6	21.87	89.18	67.0	165	209
5/30	18:59	6.46	129.65	7.2	23.04	7.8	21.34	86.66	70.0	160	204
5/30	20:45	6.5	126.59	7.1	22.76	7.7	21.59	87.74	71.0	164	213
5/31	9:00	6.39	138.79	7.6	23.37	8.1	21.88	90.39	70.0	159	193
5/31	10:57	6.42	138.66	7.6	23.40	8.1	22.07	97.04	68.0	160	189
5/31	15:15	6.4	133.40	7.3	22.31	7.6	21.98	93.11	68.4	159	191
5/31	17:45	6.36	138.49	7.6	23.15	7.9	22.63	95.52	70.4	160	196
5/31	20:22	6.36	139.83	7.5	23.09	7.9	22.24	93.85	68.4	158	193
6/1	9:05	6.3	132.83	7.3	21.82	7.4	22.15	94.61	72.4	156	157
6/1	11:57	6.36	141.63	7.7	23.07	7.9	22.04	94.44	64.8	157	145
6/1	15:26	6.34	139.98	7.5	22.47	7.6	23.01	99.90	70.8	160	141
6/1	18:22	ND	139.34	7.5	22.01	7.4	22.07	98.17	ND	160	214
6/1	21:17	ND	148.66	7.8	22.84	7.7	22.49	103.24	ND	159	216
6/2	9:11	6.3	160.43	8.2	23.35	7.7	ND	ND	74.4	163	225
6/2	12:04	6.4	164.40	8.4	23.39	7.9	ND	ND	78.0	158	227
6/2	15:00	6.38	161.40	8.2	22.89	7.6	23.63	112.13	72.8	160	224
6/2	17:58	6.58	164.05	8.4	23.22	7.7	23.82	113.48	73.6	159	200
6/2	20:53	6.51	161.77	8.2	22.96	7.5	24.23	115.33	73.2	161	206
6/4	8:45	6.37	126.02	7.1	22.69	8.1	ND	87.42	69.6	161	228

6/4	10:45	6.4	136.06	7.7	23.57	8.6	21.78	88.86	70.8	156	210
6/4	12:45	6.27	133.51	7.5	23.25	8.4	21.62	89.30	73.6	159	220
6/4	16:35	ND	164.21	8.4	23.82	8.2	23.80	111.75	ND	160	217
6/5	9:02	6.32	141.16	7.7	23.27	8.4	22.40	94.69	75.2	160	223
6/5	12:00	6.32	139.14	7.7	23.03	8.2	21.86	98.17	68.8	157	218
6/5	15:15	6.3	143.38	7.8	23.48	8.4	ND	ND	78.4	157	216
6/5	18:15	6.33	147.08	7.9	24.22	8.6	ND	ND	76.8	158	211
6/5	21:08	6.35	146.83	7.9	24.18	8.5	ND	ND	66	156	221
6/6	12:02	6.33	145.47	7.9	23.64	8.3	22.28	98.17	68.0	178	209
6/6	7:35	6.35	154.22	8.2	23.13	8.1	23.11	106.63	76.4	158	191
6/6	10:33	6.34	162.77	8.5	23.88	8.4	23.11	108.89	76.0	157	191
6/6	13:34	6.36	164.68	8.6	24.02	8.4	23.74	112.27	80.0	159	192
6/6	19:44	6.35	167.57	8.6	23.72	8.3	23.32	113.96	84.4	158	191
6/6	23:22	6.39	159.77	8.3	22.96	7.9	23.74	113.40	74.0	156	195
6/7	14:32	6.38	168.89	8.7	23.91	8.3	23.74	114.53	76.0	157	196
6/7	15:01	6.42	149.06	8.2	23.86	8.4	22.28	100.42	69.2	152	206
6/7	15:46	6.37	148.68	8.1	23.69	8.3	22.28	104.37	76.4	162	204
6/7	16:45	6.39	146.02	8.0	23.94	8.5	22.28	98.73	74.4	158	205
6/7	17:45	6.38	141.82	7.9	24.30	8.6	ND	ND	74.8	164	207

APPENDIX B

A Non-isothermal Flow Model for CO_2-Driven Cold-Water Geysers

1. Basic Assumptions

a) It is assumed that the fluid in the cold geyser is a mixture of water and carbon dioxide. Namely, only water (H_2O) and carbon dioxide (CO_2) are present there and other fluid species (e.g., other gases), if any, are not considered.

b) It is assumed that in this fluid mixture CO_2 can dissolve in water, but water does not dissolve in CO_2. This assumption can be justified because the latter process is significantly smaller in comparison with the former one in the range of temperature (10~20 °C) and pressure (0.1 ~ 2 MPa) concerned in this study.

c) The content of CO_2 in this mixture is small, i.e., its mole (or mass) fraction is significantly less than 1 (while its volume fraction can be very large because the density of the gaseous CO_2 is much smaller than that of water).

d) Flow is one-dimensional (in well).

e) Strictly, when gaseous CO_2 is present in the mixture, the pertinent gas-phase velocity is distinct from its liquid-phase counterpart because of the buoyancy effect. However, in this study we will neglect the slip effect between the two velocities, and use the routine homogeneous model, which assumes that the two-phase mixture moves in the mean velocity without slip effect. A further discussion on this issue is given in “drift-flux model” in Section 4 of this Appendix.

2. Flow Equations

The general flow equations can be found in Malekzadeh et al (2012) and Lu and Connell (2014). The flow equations given below are expressed with the homogeneous model addressed-above [Assumption (e)]. It is noted that S.I. units are used throughout the text unless stated otherwise.

Mass balance equation

$$\frac{\partial \rho_m}{\partial t}+\frac{\partial}{\partial x}\left(\rho_m v_m\right)=0 \tag{5}$$

Momentum balance equation

$$\frac{\partial}{\partial t}\left(\rho_m v_m\right)+\frac{\partial}{\partial x}\left(\rho_m v_m^2\right)+\frac{\partial p}{\partial x}=-\rho_m g \sin\theta-f_m\frac{\rho_m v_m^2}{4R_w} \tag{6}$$

In Eqs. (5) and (6), t represents time and x denotes the one-dimensional coordinate along the length or depth of the well, with upwards positive and the inlet (the bottom hole of the geyser) set to be the origin; ρ_m denote the density of the mixture, which can be further described by $\rho_m = f_L\rho_L+(1-f_L)\rho_G$, where f_L is the liquid volume fraction, ρ_L and ρ_G the density of water and CO_2, respectively. In Eqs. (5) and (6), v_m represents the average velocity of the mixture and p the pressure; f_m is the frictional coefficient of the fluid, θ the inclination angle of the well, and R_w the radius of the well.

Energy balance equation

$$\frac{\partial h_m}{\partial t}+v_m\frac{\partial h_m}{\partial x}+v_m\left(\frac{\partial v_m}{\partial t}+v_m\frac{\partial v_m}{\partial x}\right)-\frac{1}{\rho_m}\frac{\partial p}{\partial t}=-v_m\rho_m\sin\theta-\frac{q\left(T,x\right)}{\pi R_w^2 v_m}\,. \tag{7}$$

Here, h_m denotes the specific enthalpy of the mixture, q characterizes the thermal exchange between the fluid and its surroundings, which will be further discussed in Section 4 of this Appendix.

To obtain the energy balance equation for this CO_2-H_2O system, one can formally let the enthalpy of the mixture h_m be expressed by

$$h_m=h_m\left(h_L,h_G;\lambda_d\right)\,. \tag{8}$$

Here, h_L and h_G is the specific enthalpy for H_2O and CO_2, respectively, λ_d is the mole fraction of CO_2 dissolved in the mixture.

Expanding Eq. (8) with respect to λ_d into a Taylor series, one finds

$$h_m=h_m\left(h_L,h_G;\lambda_d=0\right)+\left.\frac{\partial h_m}{\partial \lambda_d}\right|_{\lambda_d=0}\lambda_d \tag{9}$$

with a first order approximation, where $\lambda_d << 1$ (Assumption-c). Clearly, $h_m\left(h_L, h_G; \lambda_d = 0\right)$ means no dissolution of CO$_2$ into water, and in this case for the immiscible system it can be expressed by $h_m\left(h_L, h_G; \lambda_d = 0\right) = z_L h_L + z_G h_G$, where z_L and z_G stand for the mole fraction of water and carbon dioxide, respectively; Clearly, $z_L + z_G = 1$. $\partial h_m / \partial \lambda_d$ in Eq. (9), denoted by Δh_s here, is actually the dissolution heat of CO$_2$ in water. Then, Eq. (9) can be described by

$$h_m = z_L h_L + z_G h_G + \Delta h_s \cdot \lambda_d . \tag{10}$$

Eq. (10) can also be expressed by the mass-based counterpart, and in that case, z_L , z_G and λ_d are the corresponding mass fractions.

Differentiating Eq. (10) one obtains $dh_m = z_L dh_L + z_G dh_G + \Delta h_s \cdot d\lambda_d + \lambda_d \cdot d\Delta h_s$, while $dh_k = C_{pk} dT - \eta_k C_{pk} dp, \quad (k = L, G)$. Here, C_{pk} ($k = L, G$) are the heat capacities at constant pressure for water and carbon dioxide, respectively, and η_k ($k = L, G$) the pertinent Joule-Thomson coefficients of them. Substitution of these equations into Eq. (7) yields

$$\Gamma_m \frac{\partial T}{\partial t} + v_m \Gamma_m \frac{\partial T}{\partial x} - \Lambda_m \frac{\partial p}{\partial t} - v_m \Lambda_m \frac{\partial p}{\partial x} + v_m \frac{\partial v_m}{\partial t} + v_m^2 \frac{\partial v_m}{\partial x} = -v_m g \sin\theta \tag{11}$$

Here, $\Gamma_m = C_{pm} + \lambda_d \left(\partial \Delta h_s / \partial T\right) + \Delta h_s \left(\partial \lambda_d / \partial T\right)$ and $\Lambda_m = \beta_m + \lambda_d \left(\partial \Delta h_s / \partial p\right) + \Delta h_s \left(\partial \lambda_d / \partial p\right)$,

while $C_{pm} = z_L C_{pL} + z_G C_{pG}$ and $\beta_m = z_L C_{PL} \eta_L + z_G C_{pG} \eta_G$.

It is noted that the dissolution (exsolution) heat, Δh_s, is usually determined by a single state argument, either by temperature or by pressure merely. Thus one has either $\partial \Delta h_s / \partial p = 0$ or $\partial \Delta h_s / \partial T = 0$ accordingly.

3. Equations of State (EoS)

a) *For water*

$$\frac{d\rho_L}{dp} = \chi_L \left(\rho_L - \rho_{L,0}\right). \tag{12}$$

Here, χ_L is the compressibility of the water and $\rho_{L,0}$ represents the density of water at a reference state.

b) *For carbon dioxide*

We use the Peng-Robinson equation of state to describe the *PVT*-behavior of carbon dioxide. Details of this equation of state can be found in the original work of Peng and Robinson (1976) or Annamalai and Puri, (2002).

4. Supplementary Relationships

a) *Drift-flux model*

The flow equations described by Eqs. (5) to (7) are based on the homogeneous model [Assumption-(e) in Section 1 of this Appendix]. Theoretically, since the gas and liquid phase velocities are distinct, one needs to incorporate a drift-flux model (Zuber and Findlay, 1965) into the pertinent flow equations, where two velocities for gas and liquid phases are involved (e.g., Malekzadeh et al, 2012). However, as discussed in Lu and Connell (2014), introducing a drift flux model (e.g., Shi et al, 2005) would lead to mathematical discontinuity or singularity at transition borders of flow patterns or when the liquid volume fraction approaches zero. Therefore, a simplified, decoupled procedure is presented here to estimate the drift-flux effect, which is addressed below.

i) First, the flow equations described by Eqs. (5) to (7) [equivalently, by Eq. (11)] are solved, which allows one to obtain the average velocity of the bubbly flow and the liquid volume fraction.

ii) Then, the relationship between the superficial gas velocity (v_{sg}) and the average velocity v_m (e.g. Hasan and Kabir, 2002)

$$f_L = 1 - \frac{v_{sg}}{C_0 v_m + v_\infty} \tag{13}$$

is used to evaluate the superficial gas velocity as f_L and v_m are known. Here, C_0 and v_∞ are two empirical constants.

b) *Dissolution (exsolution) heat of CO_2 in (from) water*

The equation given in Carroll et al (1991) is used, which is

$$\Delta_{\sin} H\left(\equiv \Delta h_s\right) = 106.56 - 6.2634 \times 10^4 \times \frac{1}{T} + 7.475 \times 10^6 \times \frac{1}{T^2} \tag{14}$$

c) *Dissolution law of CO₂*

$$x_{CO_2} = H\left(T\right) p \ \text{ or } \ x_{CO_2} = p \big/ P_{CO_2}^{Sat}\left(T\right) \tag{15}$$

Here, x_{CO_2} is the mole fraction of CO_2 dissolved in water, *H(T)* the Henry coefficient, and $P_{CO_2}^{Sat}\left(T\right)$ denotes the saturation pressure curve of CO_2.

d) *Mass balance between components*

Let $n = n_L + n_G$, where *n* is the total mole number of the system, n_L the mole number of the liquid phase and n_G the mole number of gas phase; let $\lambda = n_L \big/ \left(n_L + n_G\right)$ denote the mole fraction of liquid in the liquid-gas system. Then, from the mass balance of components one has

$$\left(1-\lambda\right) y_{H_2O} + \lambda x_{H_2O} = z_L \left(= z_{H_2O}^0\right), \tag{16}$$

$$\left(1-\lambda\right) y_{CO_2} + \lambda x_{CO_2} = z_G \left(= z_{CO_{2\partial}}^0\right). \tag{17}$$

Here, x_{H_2O} and x_{CO_2} are the mole fraction of water and carbon dioxide in liquid phase, while y_{H_2O} and y_{CO_2} are their counterparts in gas phase, respectively. In Eqs. (16) and (17), $z_{H_2O}^0$ and $z_{H_2O}^0$ are the initial mole fraction of water and carbon dioxide, respectively.

e) *Determination of mole fraction of liquid λ*

According to *Assumption- b* addressed previously, one has

$$y_{H_2O} \equiv 0 \ \text{ (H}_2\text{O does not dissolve in CO}_2\text{)} \tag{18}$$

and

$$y_{H_2O} \equiv 0 \ \text{ (gas phase is entirely composed of CO}_2\text{)} \tag{19}$$

Substitution of Eqs. (18) and (19) into Eqs. (16) and (17) gives

$$\lambda x_{H_2O} = z_{H_2O}^0 \tag{20}$$

and

$$\left(1-\lambda\right)+\lambda x_{CO_2} = z_{CO_2}^0 \tag{21}$$

With Eq. (15) one finds

$$\lambda = \left(1-z_{CO_2}^0\right) \Big/ \left\{1-\left[p \big/ P_{CO_2}^{Sat}\left(T\right)\right]\right\} \tag{22}$$

Also, one can obtain

$$x_{H_2O} = z_{H_2O}^0 \left\{1-\left[p \big/ P_{CO_2}^{Sat}\left(T\right)\right]\right\} \Big/ \left(1-z_{CO_2}^0\right) \tag{23}$$

f) *Relationship between gas mass fraction* x_{massG} *and* λ

Let $m = m_L + m_G$, where m is the total mass of the system, m_L the mass of the liquid phase and m_G the mass of gas phase; let $x_{massG} = m_G / \left(m_L + m_G\right)$ denote the gas mass fraction in the liquid-gas system. One can then have

$$x_{massG} = \left[w_{CO_2}\left(1-\lambda\right)\right] \Big/ \left(z_{CO_2}^0 w_{CO_2} + z_{H_2O}^0 w_{H_2O}\right) \tag{24}$$

Here, w_{CO_2} and w_{H_2O} is the molecular weight of carbon dioxide and water, respectively.

g) *Thermal exchange effect q*

The thermal exchange effect between a flowing fluid and its surroundings, namely, the heat flux term q in the relevant energy equation, may play a significant role in determining flow scenarios in wellbores. The simplest approach to its evaluation is based on the steady heat conduction model (e.g., Willhite, 1967; Hasan and Kabir, 2002), which can be expressed by $q = -2\pi R_{wto} U_{to}\left(T_f - T_{wb}\right)$, where R_{wto} is the tubing outside radius, U_{to} is the *overall heat transfer coefficient*, T_f is the local temperature of the fluid, and T_{wb} is the temperature at the wellbore formation interface (e.g., see Hasan and Kabir, 2002 for details).

5. Initial and Boundary Conditions

a) Initial Conditions

We use the solution for steady flow to be the initial condition. That is, simply letting $\partial(g)/\partial t \equiv 0$ in Eqs. (5), (6), and (11) and then solving the pertinent flow equations with a specific geothermal gradient, one may obtain the solution for the steady flow required.

b) Boundary Condition

The boundary flow condition is specified at the inlet of the well, i.e., at the bottomhole of the well. We assume that the fluid in the subsurface is approximately under an isenthalpic condition. Then, the variation of temperature of the fluid there can be related to pressure through

$$\left.\frac{dp}{dT}\right|_{at\ bottomhole} \equiv \frac{dp_{wb}}{dT_{wb}} = \frac{1}{\bar{\eta}_m} \tag{25}$$

Here, $\bar{\eta}_m$ denotes the effective Joule-Thomson coefficient of the H_2O-CO_2 mixture.

Suppose that the temperature of the fluid in the subsurface is perturbed (e.g., a warmer fluid coming in from deeper places), so that

$$T_{wb} = T_{wb}^0 + \delta T_{wb}(t), \tag{26}$$

Then pressure will also be perturbed accordingly. According to Eq. (25), we may (approximately) have

$$p_{wb}(t) \approx p_{wb}^0 + \frac{1}{\bar{\eta}_m}\delta T_{wb}(t) \tag{27}$$

Here, p_{wb}^0 and T_{wb}^0 is the unperturbed pressure and temperature of the fluid, respectively.

Accordingly, the perturbed velocity of fluid can be estimated in terms of

$$v_{m,wb}(t) = v_{m,wb}^0 + \frac{1}{\pi R_w^2 \eta_m} P_{indx} \cdot \delta T_{wb}(t) \tag{28}$$

where $v_{m,wb}^0$ is the unperturbed velocity of fluid, and P_{indx} is the productivity index of the wellbore.